Intrinsic Challenges in the Interpretation of Zirconium-in-Titanite Thermometry and Quartz-in-Garnet Barometry of an Ancient Subduction Zone; Cedros Island, Baja California, Mexico

by

Samuel Ray Neumann

A thesis submitted in partial fulfillment
of the requirements for the degree of
Master of Science
(Earth and Environmental Sciences)
in the University of Michigan
2026

Accepted by:

Assistant Professor Robert Holder, Advisor

Professor Nathan Niemi, Second Reader

Associate Professor Yihe Huang, Graduate Chair

I hereby grant to the Regents of the University of Michigan the non-exclusive right to retain, reproduce and distribute the deposited work (the Work) in whole or in part, in and from its electronic format. This agreement does not represent a transfer of copyright to the University of Michigan.

The University of Michigan may make and keep more than one copy of the Work for purposes of security, backup, preservation and access, and may migrate the Work to any medium or format for the purpose of preservation and access in the future. The University of Michigan will not make any alteration, other than as allowed by this agreement, to the Work.

I represent and warrant to the University of Michigan that the Work is my original work. I also represent that the Work does not, to the best of my knowledge, infringe or violate any rights of others.

I further represent and warrant that I have obtained all necessary rights to permit the University of Michigan to reproduce and distribute the Work and that any third-party owned content is clearly identified and acknowledged within the Work.

By granting this license, I acknowledge that I have read and agreed to the terms of this agreement and all related Deep Blue and University of Michigan policies.

□ Permission granted.
□ Permission granted to copy after: _____

_____
Author Signature

Abstract

We present thermobarometry and geochronology of blocks of epidote and garnet-bearing hornblendites (amphibolite facies rocks with a lack of plagioclase) from mélanges of the Cedros Island subduction complex, Baja California, Mexico, to constrain their age and the thermal gradient of the subduction interface at the time of their metamorphism. The Zr-in-rutile, Fe–Mg garnet-hornblende, and Ti-in-amphibole thermometers yield consistent temperatures ~500–630°C. However, apparent temperatures from Zr-in-titanite thermometry are ≥100°C higher. We hypothesize that during the growth of titanite, the direct replacement of rutile and the limited mobility of Zr^{4+}, Ti^{4+}, and Si^{4+} to the reaction site of titanite due to a lack of metamorphic fluid during retrogression lead to high Zr concentrations in titanite. Quartz-in-garnet thermobarometry yields a range of pressures ~0.7–1.7 GPa. Whereas previous studies have advocated for taking the maximum of such a pressure range, or statistical evaluation of means or modes, we interpret the entire range as reasonable estimates for the pressures experienced by these rocks and discuss the effect of the uncertainty in pressures on our interpretation of the geothermal gradient at the subduction zone when these rocks metamorphosed. Rutile and titanite U–Pb dates from samples with sufficient U are c. 160–150 Ma, corresponding to known Middle- to Late-Jurassic high-grade block metamorphism and exhumation along 1000s of km strike of this margin (Franciscan Complex, California; Easton metamorphic suite, Washington).

1. Introduction

The effort to constrain temperatures of metamorphic rocks has benefitted greatly from the development of trace element thermobarometers based on net-transfer equilibria among quartz, rutile, zircon, and titanite, including the Zr-in-rutile thermometer (Zack et al., 2004; Ferry and Watson, 2007; Kohn, 2020), the Zr-in-titanite thermometer (Hayden et al., 2008), the Ti-in-quartz thermometer (Wark and Watson, 2006), and the Ti-in-zircon thermometer (Watson et al., 2006). The Zr-in-rutile thermometer (Zack et al., 2004; Ferry and Watson, 2007; Kohn, 2020) is defined by the equilibrium:

(1)

This thermometer has been found to be quite useful in determining maximum metamorphic temperatures experienced by rocks spanning large ranges of metamorphic conditions (Jiao et al., 2011; Horton et al., 2016; Penniston-Dorland et al., 2018), with a common approach being to take the highest measure Zr content in rutile as the nearest estimate of peak-temperature metamorphism experienced by a rock. The Zr-in-titanite thermobarometer (Hayden et al., 2008) is defined by the equilibrium:

(2)

The incorporation of Zr into titanite is more sensitive to pressure than the incorporation of Zr into rutile. In many cases, this thermobarometer has been successful in determining metamorphic temperatures for upper-amphibolite to granulite-facies metamorphic rocks (e.g., Kohn and Corrie, 2011; Stearns et al., 2015; Holder et al., 2019).

Quartz-in-garnet elastic barometry (QuiG; Enami et al., 2007; Kohn, 2014) is a useful technique in determining pressures a rock experienced during metamorphism. The geobarometer is dependent on the remnant strain applied to quartz inclusions in garnet during exhumation due to relative differences in their compressibility and thermal expansivity. For example, quartz has greater compressibility than garnet, such that when a rock is exhumed from high pressure, a quartz inclusion will exert a positive pressure on its host garnet, proportional to the amount of decompression experienced by the rock. This creates remnant strain on the inclusion, which can be measured as a Raman peak shift. This peak shift can be used to calculate a pressure that the inclusion experienced and then used to determine what pressure the garnet experienced. This technique has been found to be quite useful across a range of garnet-bearing rocks (Wolfe et al., 2023; Spear et al., 2024; Autrey et al., 2025).

The use of trace element thermometry and QuiG barometry in tandem is highly appealing for the estimation of past *P–T* conditions owing to the apparent simplicity of their application. Ideally, one needs to measure a singular elemental concentration in one mineral (e.g., Zr in rutile or titanite, Ti in quartz or zircon) and a Raman peak shift in another mineral (e.g., quartz in garnet). While this has apparently worked well in many cases, particularly with measuring Zr concentrations in rutile (e.g., Harvey et al., 2021; Johnson et al., 2021; Wolfe et al., 2023; Spear et al., 2024), its application is often not so straight-forward, particularly when involving titanite. Temperatures calculated from Zr-in-titanite thermometry applied to blueschist-facies rocks are often anomalously high, by as much as several hundred degrees (Cruz-Uribe et al., 2018; Page et al., 2023), as well as in higher-grade rocks in which titanite grew by coronal replacement of rutile (Lucassen et al., 2010; Cruz-Uribe et al., 2018; Page et al., 2023). While QuiG can be vital in determining pressures, a wide range of results is quite common, even within apparently

equivalent growth zones of the host garnet. As such, the interpretation of metamorphic pressures depends heavily on model assumptions for how one interprets the scatter in such datasets. There are different philosophies on how to treat this range, but no singular, agreed-upon method.

In this study we look at both the Zr-in-rutile and Zr-in-titanite thermometers in conjunction with QuiG barometry in relatively high-grade hornblendites and associated blueschists from the Cedros Island subduction complex, Baja California, Mexico. U–Pb dating results for rutile and titanite in these samples showed dates of c. 160–150 Ma. These dates were determined to constrain the timing of metamorphism in our samples. We examine disparities in temperatures between the Zr-in-rutile and the Zr-in-titanite thermometers and hypothesize that these differences are caused by thermodynamic and kinetic effects. We examine the interpretation of QuiG data, and compare the different philosophies employed in other studies and how we may best interpret those data.

2. Geological Background

Cedros Island is composed of a Middle Jurassic to Late Cretaceous subduction complex "lower-plate" structurally overlain by an ophiolite and forearc sediments "upper-plate" (Figure 1; Busby et al., 1998; Kimbrough and Moore, 2003). Overlying sedimentary rocks consist of volcaniclastic deposits and marine turbiditic strata. Normal faulting in the upper plate has exhumed structurally lower, high-pressure subduction-complex rocks. The Cedros Island Ophiolite (c. 170 Ma) is interpreted to be a supra-subduction zone ophiolite, reflecting major extension and rifting in the fore-arc basement (Kimbrough and Moore, 2003). The "lower plate" subduction complex consists of low-grade (5–8 kbar, 170–300°C) blueschist-facies metasedimentary and metabasic, abyssal and trench rocks (Kimbrough, 1985; Sedlock, 1988) with a volcanosedimentary matrix. These "lower-plate" rocks are separated from the overlying ophiolite by a serpentinite-matrix mélange containing exotic blocks, including greenschist, lawsonite-blueschist, epidote-blueschist, amphibolite, epidote-amphibolite, garnet-amphibolite, and eclogite facies blocks (Kilmer, 1977; Sedlock, 1999). The mélange varies in thickness (meters to 10s of meters) with foliation broadly parallel to its margins (Sedlock, 1988). Similar instances of mélange are found within the lower plate, locally along nappe contacts near Punta Prieta (Sedlock, 1988). The metasedimentary matrix of the lower plate also contains exotic blocks in isolation and in groupings—partially to completely surrounded by chlorite-actinolite or serpentinite rinds—that are not associated with discrete faults or shear zones. These are interpreted as olistostromes (e.g., Wang et al., in press), analogous to some high-pressure block localities in the along-strike correlative Franciscan Complex of California (Wakabayashi, 2015). Amphibole and mica $^{40}Ar/^{39}Ar$ ages for the amphibolite blocks are 170–163 Ma and 115–100 Ma for the blueschist blocks (Baldwin and Harrison, 1992).

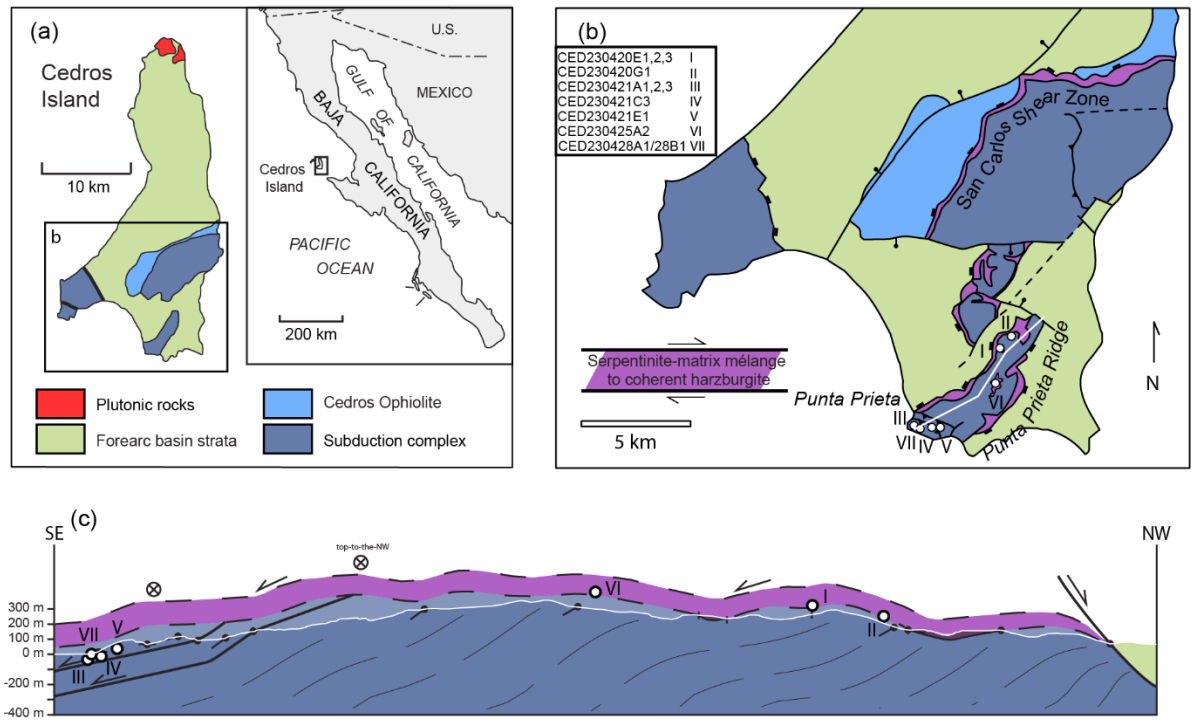


Figure 1: (a): Map of Cedros Island with broad stratigraphic units. (b): Studied sample locations are marked with roman numerals on the Punta Prieta Ridge. The purple unit shown, includes the serpentinite-matrix mélange and overlying, variable exposures of harzburgite. These units are not differentiable at this scale, so they are combined into a singular unit. There is a distinct lithologic difference between these two units. There is no harzburgite within the exotic block mélange itself. (c): Cross section showing the lower-plate consisting of blueschist facies volcanosedimentary rock in blue, the serpentinite-matrix mélange to coherent harzburgite in purple, and forearc basin strata in green. The pale blue colors represent the lower plate extrapolated above the transect.

3. Sample descriptions

The studied samples are epidote (±garnet) hornblendites and epidote (±lawsonite) blueschists collected from Punta Prieta Ridge, the southernmost exposure of the lower-plate subduction complex on Cedros Island: Subterrane 3 of (Sedlock, 1988). Detailed descriptions of each sample are given below, grouped by general structural position. The following samples are exotic blocks collected from the structurally highest serpentinite-matrix mélange, which separates the predominantly blueschist-facies subduction complex of Punta Prieta Ridge from the overlying coherent harzburgite, interpreted to be the base of the Cedros Ophiolite.

CED230420E1 (Garnet-epidote hornblendite): Major minerals in this sample are amphibole, garnet, titanite, and epidote. The amphibole tends to show slight pleochroism. Garnets show distinct chemical growth rings and are rich in inclusions (epidote and amphibole dominantly, with some quartz). Titanite are (hyp)idioblastic and up to ~3000 μm across. Epidote is seen within garnets as inclusions and within the matrix. Rutile is present as rare inclusions in titanite. Quartz is a trace mineral in the matrix. The sample contains abundant, relatively large (up to ~1000 μm) apatite. A weak foliation is defined by preferred orientation of amphibole grains.

CED230420E2 (Garnet-epidote hornblendite): is an exotic block collected from the same locality as 20E1. Major minerals in this sample are amphibole, epidote, and garnet. Garnets have inclusions of epidote, amphibole, and quartz. Garnet tends to be fractured with distinct cores defined by a lack of inclusions. Fine-grained titanite is pervasive throughout the sample. Minor quartz is present in the amphibole matrix. Minor apatite and oxides are also seen. A weak foliation is defined by preferred orientation of amphibole grains that wraps garnet.

CED230420E3 (Epidote amphibolite): is an exotic block collected from the same locality as 20E1 and 20E2. Major minerals in this sample are light-brown hornblende, epidote, and white/pale-gray mats of a fine-grained mineral interpreted to be a replacement of plagioclase. Titanite is a minor mineral, locally preserving fine-grained inclusions of rutile in its cores. A foliation is defined by preferred orientation of amphibole and mineralogical banding.

CED230420G1 (Epidote-actinolite-chlorite schist): Major minerals in this sample are light to emerald, green acicular actinolite with epidote, and chlorite. Minor amounts of titanite and rutile and trace amounts of white mica, plagioclase, quartz, and oxides are present. Epidote ranges from fine to coarse-grained. Titanite exists as coronae around ~10–30 μm rutile grains as well as separate, disseminated grains (~10-20 μm) in the matrix. A single large, relict, and heavily altered garnet was observed in thin section. Coarser-grained, lighter blue-green actinolite is associated with local carbonate veins.

CED230425A2 (Lawsonite-epidote-blueschist): Major minerals in this sample are glaucophane, lawsonite, and epidote. Minor amounts of calcite, white mica, oxides and titanite are present. Some layers rich in white mica are seen throughout. Green amphibole layers are thought to be prehnite. The sample tends to be fine-grained but has coarser domains throughout.

The following samples are from the southwest end of Punta Prieta ridge (Punta Prieta proper), in or near large quarries. Observations from the quarry walls as well as non-quarried exposures indicate that the (garnet-)hornblendite blocks occur both in isolation and in groupings, surrounded by serpentine-chlorite-actinolite-talc schists within the volcanosedimentary matrix of the lower plate. With the exception of sample 21C3, these exposures of mélange do not show

lateral continuity indicative of a structural boundary; they are apparently isolated within the otherwise coherent volcanosedimentary schist that comprises the dominant lithology of Punta Prieta.

CED230421A1 (Garnet-epidote hornblendite), quarry float: Major minerals in this sample are amphibole, garnet, and epidote. Minor to trace amounts of rutile, titanite, quartz, stilpnomelane, chlorite, and oxides are present. Garnet contains inclusions of quartz, hornblende, epidote, and more rarely rutile.

***CED230421A2 (Garnet-epidote-amphibolite), quarry float*:** Major minerals in this sample are amphibole, garnet, epidote. Rutile, titanite, chlorite, plagioclase, and quartz are minor in abundance. White mica is seen in trace amounts. Amphibole is coarse-grained and euhedral to subhedral. Garnets are very coarse-grained, partially altered, and include epidote and amphibole. Epidote is coarse-grained and euhedral. Rutile grains are quite large and show titanite rims. Titanite is large and euhedral.

***CED230421A3 (Garnet-epidote-hornblendite), quarry float*:** Major minerals in this sample are hornblende, garnet, and epidote. Minor amounts of titanite, quartz, plagioclase, chlorite, white mica, and apatite. Trace amounts of white mica. There is what looks to be rutile, but it is completely replaced by titanite. Chlorite commonly replaces the amphibole and garnet. Hornblendes are coarse and euhedral. Garnets are coarse and contain micro inclusions such as epidote, quartz, and hornblende. Titanite is made up of small aggregates (<1 um).

***CED230428A1 (Garnet-epidote hornblendite), isolated block*:** Major minerals in this sample are garnet, hornblende, and epidote. Rutile and quartz are seen in minor amounts. Rutile tends to be

rimmed by titanite. Garnet is extremely coarse and inclusion rich. Hornblende is coarse-grained and euhedral. Epidote is coarse-grained and subhedral.

***CED230428B1 (Garnet-epidote hornblendite), isolated block*:** Major minerals in this sample are garnet, hornblende, titanite and epidote. Minor amounts of quartz and plagioclase are present. Amphibole is coarse, and ranges from green to brown in color. Garnet in this sample is quite large and inclusion rich specifically including quartz, epidote, and amphibole. Titanite is medium-grained and found in the matrix.

CED230421C3 (Garnet-epidote hornblendite): was collected from a layer of serpentine-chlorite-actinolite-talc schist (~5 km thick) interpreted as a minor thrust contact between nappes of the lower plate exposed near Punta Prieta by (Sedlock, 1988). Due to its position in the lower plate, it is lithologically akin to, but structurally distinct from the serpentinite mélange of 20E1. Major minerals in this sample are hornblende, garnet, rutile, and titanite. Minor minerals include chlorite and white mica. Hornblende is coarse grained and tends to be green to brown. Garnets are quite large and contain inclusions of quartz, epidote, and amphibole. Minor chlorite is seen on the edges of garnet. Rutile is very coarse grained and rimmed with titanite. Large, euhedral titanite are also present in the matrix.

CED230421E1 (Epidote-blueschist): is an isolated exotic block collected just beneath a thrust contact internal to the subduction complex, separating the distinctly dark volcanosedimentary rocks of Punta Prieta (to the southwest) from the lighter, predominantly red to brown sandstones and siltstones that comprise the majority of the ridge toward the northeast (Sedlock, 1988; Wang

et al., in press). Major minerals in this sample are glaucophane, chlorite, and epidote. Glaucophane is coarse and ranges from blue to colorless. Minor amounts of titanite and quartz. Trace amounts of white mica and stilpnomelane. The chlorite is also rather coarse and is oriented the same as the glaucophane. Titanite is coarse-grained. Epidote is extremely common and very fine-grained. Quartz is seen in veins, and as a small constituent of the matrix. Chlorite can be seen replacing glaucophane. Both glaucophane and chlorite define the foliation of this sample.

4. Methods

4.1 Rutile EPMA Methods

We measured compositions of rutile in thin section using a CAMECA SX100 Electron Microprobe with an accelerating voltage of 15kV, a beam current of 250 nA, and an estimated beam diameter of 5 μm. Concentrations of Zr, Ti, V, Cr, Nb, and Fe were measured. Zr was measured via its Lα* emission line with PET and LPET crystals, with a peak count time of 800 seconds, and standardized with a synthetic $ZrSiO_4$ crystal. Ti was measured via its Kα emission line with a LLiF crystal, with a peak count time of 10 seconds, and standardized with a synthetic TiO_2 crystal. V was measured via its Kα** emission line with a LLiF crystal, with a peak count time of 120 seconds, and standardized with a synthetic YVO_4 crystal. Cr was measured via its Kα emission line with a LLiF crystal, with a peak count time of 120 seconds, and standardized with a synthetic Cr_2O_3 crystal. Nb was measured via its Lα emission line with a PET crystal, with a peak count time of 400 seconds, and standardized with a synthetic $LiNbO_3$ crystal. Fe was measured via its Kα emission line with a LLiF crystal, with a peak count time of 120 seconds, and standardized with a natural Elba Hematite sample. Concentrations of Zr, Cr, Fe, and Nb were corrected by using the "blank" correction of (Donovan et al., 2011), by following the method for combined MAN/blank analyses from (Donovan et al., 2016). The blank standard was a synthetic rutile with 0 μg/g Zr, Cr, Fe, and Nb as verified by LA-ICP-MS at the University of Michigan.

Zr-in-rutile temperatures were calculated using the "combined" calibration of (Kohn, 2020), which uses empirical data from natural rocks (T<800°C) to better constrain extrapolation of experimental data (T>800°C) to lower temperatures. Mean weighted averages of Zr

concentrations in each rutile were used as the Zr concentration for each analysis. Calculations assume unity activities of zircon and silica. Uncertainties in calculated temperatures were propagated from the covariance matrix of the (Kohn, 2020) thermometer as well as the analytical uncertainties of the Zr measurements.

4.2 LA-ICP-MS Rutile U–Pb

U–Pb dates in rutile were measured in thin section at University of California, Santa Barbara following the methods outlined in (Kylander-Clark et al., 2013; Kylander-Clark, 2017). The laser used was an ESL ImageGeo, with U–Pb measured by a Nu Instruments P3D Plasma high-resolution MC-ICP-MS system. The rutile was ablated using a 25 μm spot, analyzed at 7 J/cm^2 and 5 Hz for 12 seconds preceded by a 2 shot preablation and 12 second washout. Kragerø was used as the primary reference material.

4.3 LA-ICP-MS Titanite U–Pb, and Zr thermometry

U–Pb dates and Zr concentrations in titanite were measured in thin section at the University of Michigan using an Agilent 7900 quadrupole ICP-MS with an ESI NWR193 excimer laser-ablation system. Analyses consisted of a 4 s ablation, using a fast-washout tubing system (~100 ms washout to 1% of peak signal), with a spot size of 25 or 15 μm, repetition rate of 50 Hz, a fluence of ~0.8 J/cm^2, and four cleaning shots followed by four seconds of baseline collection. Measured masses and integration times were ^{47}Ti (0.02 s), ^{90}Zr (0.02 s), ^{206}Pb (0.023 s), ^{207}Pb (0.064 s), and ^{238}U (0.02s). Data were collected using standard-sample bracketing and processed using the commercially available software Iolite version 4. The primary reference material for

U–Pb dating was NIST612 with OLT, BLR, and MKED as secondary reference materials. The primary reference material for Zr, U, and Pb concentrations was NIST612 (GeoRem recommended values), using Ti as an internal standard with an assumed concentration of 24 wt% in the unknown titanite. Temperatures were calculated using the Zr-in-titanite thermometer of (Hayden et al., 2008) with uncertainties propagated in quadrature from the thermometer coefficients and measured Zr uncertainty. Initial thermometry calculations were done assuming activities of unity for titania and silica, based on the presence of rutile and quartz in the samples (an assumption that will be revisited in the discussion).

4.4 QUIG

Raman spectra of quartz inclusions in garnet and the garnet itself were collected at the University of Michigan using a Horiba XploRA PLUS Raman system. Spectra were collected at ambient conditions using a laser with an excitation of 532 nm and a grating of 1800 gr/mm. The detector was a SIN-EM FIVIS. The objective view was 50x. Spectra were collected for between 15–25 seconds at 5 accumulations. Samples were examined in both thick (100 μm) and thin (30 μm) sections. The majority of identified inclusions were only a few micrometers in diameter (all <10 μm). Given the small grain size of the inclusions, samples were measured in thin section, which provided greater optical clarity than thick sections. Care was taken to consider only grains internal to the thin sections to avoid relaxation of elastic strain associated with proximity to the samples' surfaces. Spectra were externally standardized using the 464 cm^{-1} peak as measured in a crystalline piece of free quartz. To further ensure measurement accuracy, a CFL bulb was placed 5 feet from the spectrometer during analysis, producing a distinct 482 cm^{-1} Hg emission line in each unknown spectrum for use as an internal standard (Izraeli et al., 1999). Due to the small

grain sizes of the entrapped quartz, quartz spectra were commonly contaminated by garnet. To mitigate this challenge, garnet was measured immediately adjacent to quartz then differenced from the raw quartz spectra (Cizina et al., 2023) using a MATLAB code provided by M. Kohn. These data were then run through StRAinMAN (Angel et al., 2019) to determine the peak shifts, which were, in turn, input into EntraPT (Mazzucchelli et al., 2021) to generate isomekes (a line through *P*-*T* space that represents entrapment conditions of a mineral inclusion within a host mineral) for each sample.

5. Results

5.1 Zr in rutile and other trace elements

All rutile EPMA data are presented in Supplementary Table S1 and summarized in Table 1. Zr-in-rutile temperatures are shown in Figure 2. Confidence intervals are based on 1-sigma analytical errors.

Rutile from garnet-epidote hornblendites (21C3, 21A2, 28A1, 20E1, and 21A1) yielded V concentrations ranging from 732.6 ± 6.9 to 3548.3 ± 12.8 μg/g, Cr concentrations ranging from 188.7 ± 13.1 to 1418.2 ± 14.9 μg/g, Fe concentrations ranging from 1462.5 ± 16.5 to 8785.4 ± 24.6 μg/g, Nb concentrations ranging from 180.7 ± 20.5 to 1048.1 ± 21.8 μg/g, and Zr concentrations ranging from 51.4 ± 13.9 to 379.4 ± 14.6 μg/g corresponding to Zr-in-rutile temperatures of 494 ± 42°C to 675 ± 13°C.

Rutile from samples without garnet (20G1 and 20E3) yielded V concentrations ranging from 566.9 ± 6.3 to 1418.2 ± 8.4 μg/g, Cr concentrations ranging from 75.9 ± 12.7 to 2208.4 ± 16.1 μg/g, Fe concentrations ranging from 452.4 ± 15.0 to 4349.2 ± 20.4 μg/g, Nb concentrations ranging from 74.5 ± 21.1 to 2859.6 ± 25.2 μg/g, and Zr concentrations ranging from 77.3 ± 14.3 to 189.1 ± 14.3 μg/g corresponding to Zr-in-rutile temperatures of 522 ± 30°C to 612 ± 17°C.

Table 1: Ranges of measured trace element concentrations from rutile using EPMA analysis. Reported uncertainties correspond to 1 standard deviation.

Sample	CED230420E1	CED230420E3	CED230420G1	CED230421A1	CED230421A2	CED230421C3	CED230428A1
V (µg/g)	1004.2 ± 7.6–1483 ± 8.7	707.9 ± 6.7–1418.2 ± 8.4	566.9 ± 6.3–1235.8 ± 7.9	732.6 ± 6.9–1943.3 ± 9.5	1403.0 ± 8.3–2207.1 ± 9.9	2138.1 ± 10–3548.3 ± 12.8	986 ± 7.6–1703.9 ± 9.2
Cr (µg/g)	444.3 ± 13.2–977.3 ± 14.2	863.6 ± 13.9–2208.4 ± 16.1	75.9 ± 12.7–510.9 ± 13.3	213.9 ± 12.8–1269.0 ± 14.5	291.4 ± 13.0–1418.2 ± 14.9	188.7 ± 13.1–521.7 ± 13.6	346.4 ± 13.4–741.6 ± 14
Fe (µg/g)	1534.0 ± 15.34 –2889.5 ± 17.9	452.4 ± 15.0–4118.9 ± 19.8	2596.8 ± 18.2–4349.2 ± 20.4	1633.7 ± 16.5–8785.4 ± 24.6	2386.0 ± 17.9–4197.5 ± 20.1	1462.5 ± 16.5–4178.9 ± 20.1	2175.9 ± 17.6–4598.2 ± 20.7
Nb (µg/g)	671 ± 21.3–1027.6 ± 22.2	856.2 ± 21.3–2859.6 ± 25.2	74.5 ± 21.1–1989 ± 24.7	316.3 ± 20.4–1048.1 ± 21.8	336.1 ± 21.6–992.7 ± 22.7	180.7 ± 20.5–905.4 ± 21.8	189.1 ± 20.6–752.0 ± 21.6
Zr (µg/g)	107.7 ± 14.3– 179.7 ± 14.4	77.3 ± 14.3–137.7 ± 14.4	80.1 ± 14.2–189.1 ± 14.3	51.4 ± 13.9–156.4 ± 14.06	56.1 ± 14.2–268.2 ± 14.4	89.1 ± 14.4–379.4 ± 14.6	119 ± 14.4–279.6 ± 14.5
T (°C)	546 ± 24–586 ± 19°C	522 ± 30–564 ± 21°C	544 ± 29–612 ± 17°C	494 ± 42–574 ± 20°C	520 ± 39–642± 15°C	552 ± 27–675 ± 13°C	574 ± 23–646 ± 14°C

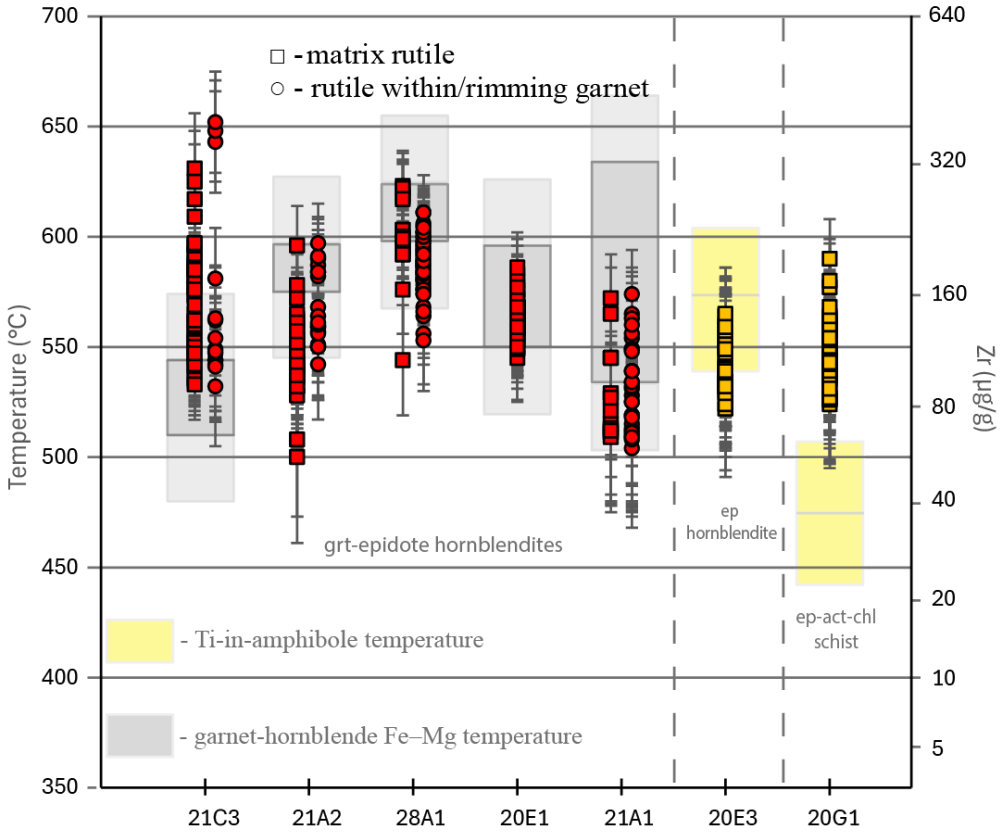


Figure 2: Peak *T* estimates among Zr-in-rutile, Fe–Mg garnet hornblende, and Ti-in-amphibole thermometers Individual Zr-in-rutile analyses temperatures are shown for each sample. Squares represent rutile found in the matrix while circles represent rutile found within or in contact with garnet. Samples in red are classified as garnet bearing hornblendites, samples in orange are samples that do not contain garnet. Fe–Mg garnet–hornblende temperatures are shown as grey boxes which include a 95% CI uncertainty. Ti-in-amphibole temperatures are shown as yellow boxes with a minimum error estimate of ± 35°C.

5.2 Zr, U, and Pb in titanite

All titanite data are presented in Supplementary Table S2 and summarized in Table 2.

Titanite from garnet-hornblendite samples yielded U concentrations ranging from 0 to 15.03 ± 1.12 μg/g and Zr concentrations ranging from 3.18 ± 0.52 to 564.72 ± 12.97 μg/g, corresponding to 1 GPa temperatures of ~576–892°C assuming quartz, rutile, and zircon activities of unity.

Titanite from epidote-hornblendite samples yielded U concentrations ranging from 0 to 9.4 ± 0.98 μg/g and Zr concentrations ranging from 5.75 ± 0.6 to 1213.95 ± 52.69 μg/g, corresponding to 1 GPa temperatures of ~592–842°C assuming quartz, rutile, and zircon activities of unity.

Titanite from lawsonite and epidote blueschist samples yielded U concentrations ranging from 0 to 2.92 ± 0.23 μg/g and Zr concentrations ranging from 0.86 ± 0.18 to 489.09 ± 14.5 μg/g, corresponding to 1 GPa temperatures of ~546–834°C assuming quartz, rutile, and zircon activities of unity.

Titanite from the greenschist sample 20G1 yielded U concentrations ranging from 0 to 0.5 μg/g and Zr concentrations ranging from 11.32 ± 2.89 to 352.6 ± 24.5 μg/g, corresponding to 1 GPa temperatures of ~591–754°C assuming quartz, rutile, and zircon activities of unity.

Samples	20E3	21E1	20E1	21A2	21C3	28A1	21A1	21A3	20G1	20C1	25A2
U(µg/g)	0.015 ± 0.009 – 9.4 ± 0.98	0.02 ± 0.01 – 2.92 ± 0.23	0.53 ± .05 – 12.4 ± 0.31	0 – 1	1.17 ± .01 – 14.8 ± 0.39	0 – 0.86	0.17 ± 0.04 – 15.03 ± 1.12	0.37 ± 0.07 – 4.02 ± 0.19	0 – 0.5	0.18 ± .04 – 2.41145 ± 0.6	0.05 ± 0.01 – 31.0 ± 10.5
Pb(µg/g)	0.30 ± 0.05 – 23.52 ± 1.6	0.26 ± 0.1 – 14.32 ± 1.86	1.2 ± 0.18 – 11.9 ± 1.15	0.3 ± .09 – 5.1 ± 2.0	.34 ± .08 – 3.8 ± .16	0.8 ± .1 – 9.46 ± .8	0.71 ± 0.06 – 24.13 ± 0.86	0.91 ± 0.09 – 20.32 ± 2.31	0.39 ± .08 – 23.3 ± 1.18	3.11 ± .25 – 11.78 ± 1.1	4.58 ± 0.27 – 73.62 ± 7.39
Zr(µg/g)	7.75 ± 0.48 – 1213.95 ± 52.69	5.11 ± 0.46 – 169.8 ± 54.4	13.5 ± 0.4 – 240.3 ± 4.2	3.18 ± .52 – 222.8 ± 5.4	9.88 ± .56 – 564.72 ± 12.97	6.99 ± .4 – 275 .5 ± 4.8	11.52 ± 0.44 – 80.58 ± 19.0	17.6 ± 1.04 – 824.6 ± 54.6	11.32 ± 2.89 – 352.6 ± 24.5	2.66 ± 0.47 – 244.1 ± 113.8	0.86 ± 0.18 – 489.09 ± 14.5
T(°C)	576 – 828	610 – 772	650 – 792	592 – 787	637 – 842	622 – 800	643 – 733	661 – 867	591 – 754	586 – 792	546 – 834

Zr-in-titanite temperatures shown below.

Table 2: Titanite trace element co

Samples	20E3	21E1	20C1	25A2	20G1
U(µg/g)	0.015 ± 0.009 – 9.4 ± 0.98	0.02 ± 0.01 – 2.92 ± 0.23	0.18 ± .04 – 2.41145 ± 0.6	0.05 ± 0.01 – 31.0 ± 10.5	0 – 0.5
Pb(µg/g)	0.30 ± 0.05 – 23.52 ± 1.6	0.26 ± 0.1 – 14.32 ± 1.86	3.11 ± .25 – 11.78 ± 1.1	4.58 ± 0.27 – 73.62 ± 7.39	0.39 ± .08 – 23.3 ± 1.18
Zr(µg/g)	7.75 ± 0.48 – 1213.95 ± 52.69	5.11 ± 0.46 – 169.8 ± 54.4	2.66 ± 0.47 – 244.1 ± 113.8	0.86 ± 0.18 – 489.09 ± 14.5	11.32 ± 2.89 – 352.6 ± 24.5
T(°C)	576 – 828	610 – 772	586 – 792	546 – 834	591 – 754

Table 2: Titanite trace element concentrations shown for U, Pb, and Zr. Corresponding range of Zr-in-titanite temperatures shown below.

5.3 U–Pb rutile and titanite

The U–Pb rutile data are presented in Table S3 and shown in Figure 3. Data for sample 21C3 (Figure 3) show a lower intercept date of 155 ± 4 Ma (2se). Samples 20D1, 20E1, 20E3, 20G1, 27B4, 21A1, 21A2, 21A8, 21D1, and 28A1 were also measured, but U concentrations were too low to produce a meaningful U–Pb date.

The U–Pb titanite data are presented in Table S2 and shown in Figure 3. Data define discordant arrays consistent with mixing between different proportions of common and radiogenic Pb as functions of initial U/Pb ratio. The $^{207}Pb/^{206}Pb$ intercepts are ~0.84–0.88, consistent with the expectations of the Stacey and Kramers model for terrestrial Pb evolution (Stacey and Kramers, 1975). Three samples yielded resolvable lower intercept dates: sample 21C3, 149.7 ± 8.7 Ma (2se); sample 21A1, 148 ± 15 Ma (2se); and sample 20E1, 165 ± 17 Ma (2se). Samples 20C1, 21B1, 25A2, 21A2, 28A1, 20E3, 20G1, 21A3, and 21E1 were also measured, but all too low in U to produce a meaningful U–Pb date. The titanite and rutile U–Pb dates of sample 21C3 (149.7 ± 8.7 Ma and 155 ± 4 Ma, respectively) are indistinguishable.

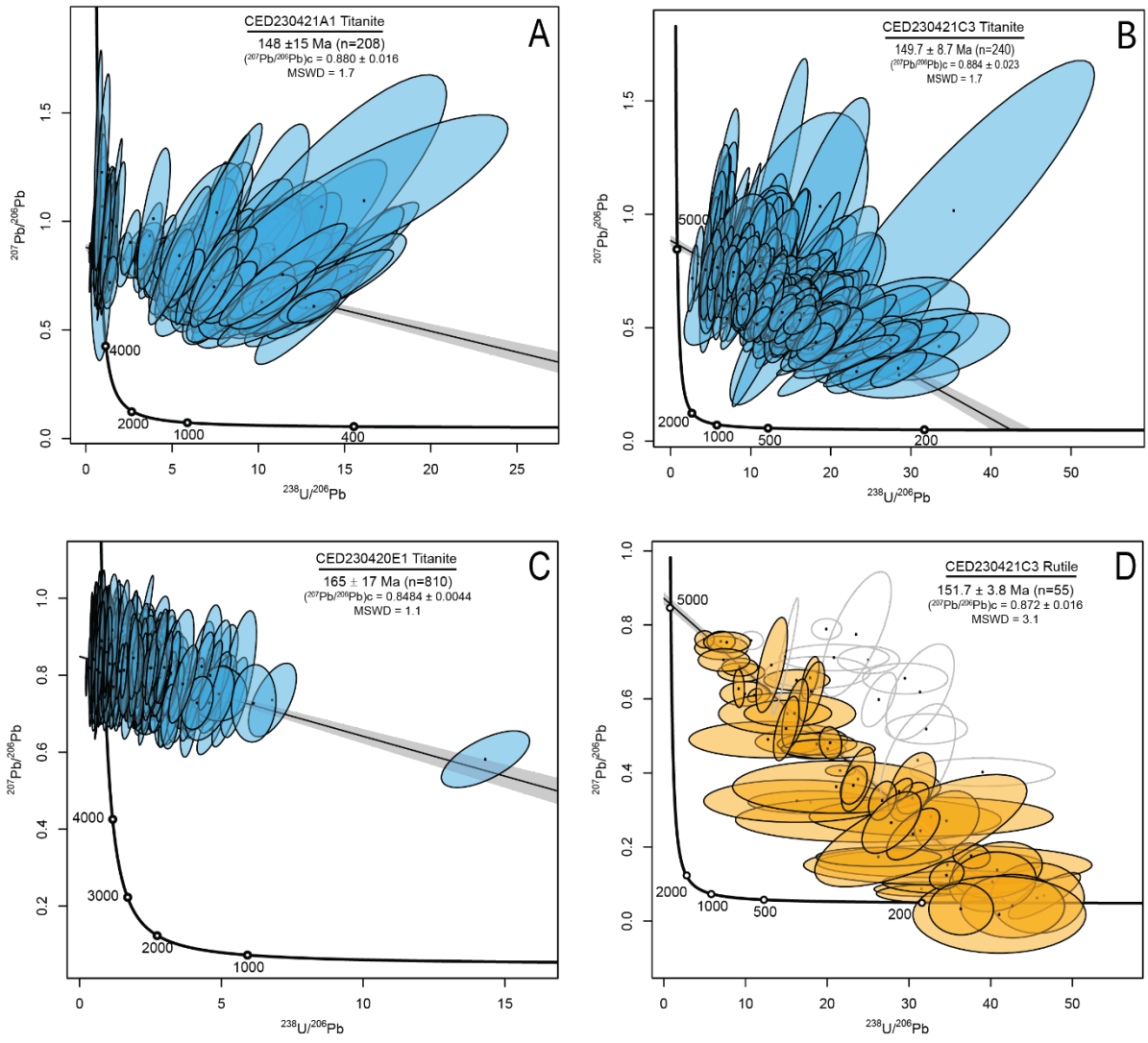


Figure 3: U–Pb concordia diagrams for titanite from samples (A) 21A1 (B) 21C3, and (C) 20E1. U–Pb concordia diagram for rutile from sample 21C3. Hollow ellipses omitted from regression in panel (D). All uncertainties are 2se.

5.4 QuiG

Calculated strain data and quartz standard measurements are compiled in tables S4 and S5. Calculated isomekes for quartz inclusions in garnet are presented in Table S6 and Figure 4. A summary of the data from each sample is included in Table 3. Calculated pressures of quartz entrapment in garnet are ~0.9–1.25 GPa (20E1), ~1.25–1.6 GPa (20E2), ~0.95–1.25 GPa (21A1), ~1.0–1.7 GPa (21A3), ~0.8–1.3 GPa (21C3), ~0.7–1.25 GPa (28B1). The quartz measured in each sample were located near the rims of garnet, at least three radius lengths away from other inclusions, cracks, or the edge of the garnet grain. Quartz grains analyzed were generally equant. The variability in pressures is not correlated with the quartz grains relative proximities to the edge of the garnet grain, other inclusions, or cracks in the garnet.

Table 3: Raman peak shifts for each inclusion measured for QuiG. V_{128}, V_{206}, V_{464} measured in cm^{-1}. *P* is calculated at a constant *T* of 575°C.

Quartz inclusion Raman measurements							
Sample	Inc #		V_{128}	V_{206}	V_{464}	P	2SE
CED230428B1		1	128.405	213.1047	465.6951	1.156	0.056
		2	126.3513	204.8064	462.8667	0.602	0.123
		3	126.4379	204.578	463.3845	0.563	0.171
		4	127.8046	207.6807	464.898	0.712	0.121
		5	128.2812	210.2633	464.4313	0.942	0.055
		6	129.3198	211.3616	465.9314	0.939	0.044
CED230420E1		1	129.8346	213.5065	467.2132	1.104	0.162
		2	128.4703	212.0985	465.3999	1.081	0.041
		3	129.5229	212.0606	466.1755	0.985	0.057
		4	130.2409	213.3909	466.5387	1.067	0.157
		5	131.1378	215.8552	468.1366	1.2	0.131
		6	130.3751	215.9704	467.8988	1.258	0.03
		7	130.5329	215.2169	467.624	1.199	0.144
CED230420E2		1	129.8645	216.5169	467.3962	1.576	0.059
		2	130.0003	213.9958	466.9166	1.337	0.17
		3	130.8765	216.8062	468.2122	1.478	0.197
		4	130.5969	215.4361	467.6449	1.425	0.203
		5	129.5623	213.4161	466.4098	1.319	0.154
		6	129.6778	214.3823	466.4105	1.415	0.197
		7	129.1223	211.2068	465.8803	1.139	0.105
CED230421A3		1	129.408	214.5061	466.3783	1.221	0.05
		2	127.8754	215.649	466.5182	1.404	0.247
		3	129.454	214.8493	466.6758	1.24	0.023
		4	128.6448	215.7272	466.5841	1.374	0.105
		5	129.1844	212.7046	466.5957	1.043	0.05
		6	129.8986	218.8302	466.8523	1.636	0.16
		7	130.5929	218.253	465.6918	1.596	0.475
		8	130.9433	215.7209	467.5889	1.221	0.177
CED230421A1		1	129.0664	212.1719	465.9439	1.025	0.012
		2	130.0558	216.2356	467.4414	1.319	0.045
		3	128.7916	215.1098	466.9412	1.286	0.141
CED230421C3		1	130.2054	210.147	467.0643	0.75	0.019
		2	128.4076	214.5014	466.9536	1.239	0.222

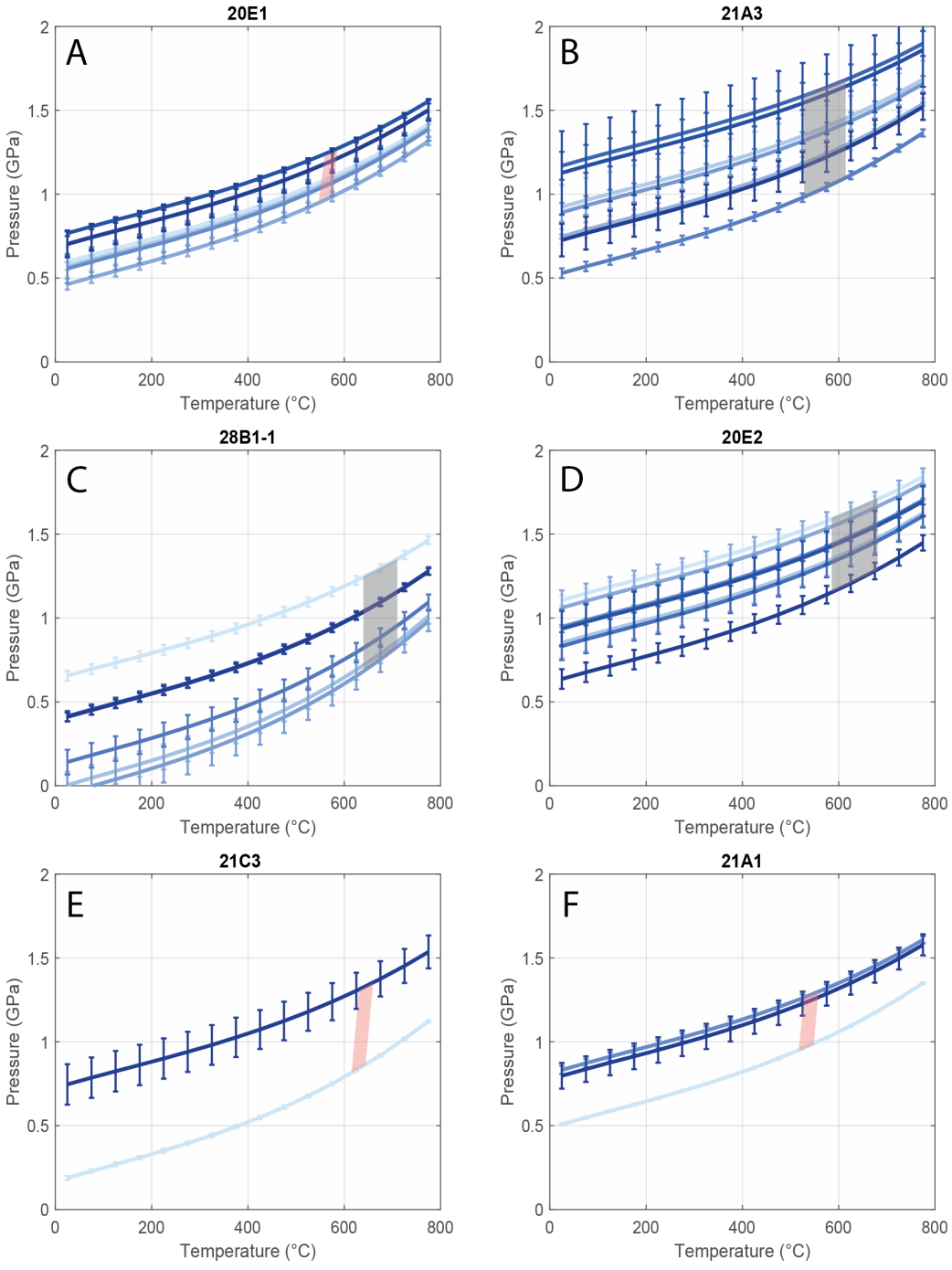


Figure 4: Isomekes calculated from QuiG analyses for individual inclusions within each sample. Uncertainty on the isomekes is one estimated standard deviation. The red polygons represent temperatures determined via Zr-in-rutile

thermometry, while the gray polygons represent temperatures determined via Fe–Mg garnet-hornblende thermometry.

Table 4: Summary of U–Pb dates and thermobarometry of the studied samples.

samples	U-Pb date (Ma)[a]	maximum Zr-in-rutile *T* (°C)[b]	minimum Zr-in-titanite *T* (°C)[c]	QuiG *P* (GPa)[d]	Fe–Mg garnet–hornblende *T* (°C)[e]	Ti-in-amphibole *T* (°C)[f]	GPHQ *P* (GPa)[g]
Ced230420E1 (grt–ep hornblendite)	Titanite: 165 ± 17	563°C ± 13°C	651 ± 15	~0.9–1.25	550–595 ± 30°C	586 ± 35°C	no pl
Ced230420E2 (grt–ep hornblendite)	ttn too fine no rut	no rt	ttn too fine	~1.25–1.6	590–670 ± 30 °C	579 ± 35°C	no pl
Ced230420E3 (ep hornblendite)	too low U	544°C ± 14°C	626 ± 14.2	no grt	no grt	572 ± 35°C	no grt
Ced230420G1 (ep–act–chl schist)	too low U	550°C ± 13°C	639 ± 14.6	no grt	no grt	477 ± 35°C	no grt
Ced230425A2 (lws blueschist)	too low U	no rt	546 ± 14.2	no grt	no grt	No Ca amph	no grt
Ced230421A1 (grt–ep hornblendite)	Titanite 148 ± 15	533 °C ± 14°C	625 ± 14.4	~0.95–1.25	530–630 ± 30 °C	585 ± 35°C	no pl
Ced230421A2 (grt–ep amphibolite)	too low U	558 °C ± 14°C	603 ± 14	no qtz inclusions	580–590 ± 30°C	541 ± 35°C	~1.7–2.3 ± 0.1
Ced230421A3 (grt–ep hornblendite)	too low U	rt replaced by ttn	662 ± 15	~1.0–1.7	530–615 ± 30°C	582 ± 35°C	no pl
Ced230421C3 (grt–ep hornblendite)	Titanite: 149.7 ± 8.7 Rutile: 154.7 ± 6.1	636 °C ± 13°C	637 ± 14.6	~0.8–1.3	510–545 ± 30°C	585 ± 35°C	no pl
Ced230421E1 (ep blueschist)	too low U	no rt	610 ± 14.2	no grt	no grt	No Ca amph	no grt
Ced230428A1 (grt–ep hornblendite)	too low U	620°C ± 13°C	623 ± 14.2	few qtz inclusions	600–620 ± 30°C	596 ± 35°C	no pl
Ced230428B1 (grt–ep hornblendite)	no rut ttn too fine	no rt	ttn too fine	~0.7-1.25	640–710 ± 30°C	664 ± 35°C	no pl

a: U–Pb ages (Ma) ±2se **b**: All temperatures calculated at 1 GPa with ±2se **c**: All temperatures calculated at 1 GPa; 2se is shown **d**: 20E1, 21C3, and 21A1 *P* is calculated using Zr-in-rutile *T*. 20E2, 21A3, and 28B1 are calculated using Fe–Mg garnet-hornblende exchange thermometer *T* **e**: Calculated using pairwise analyses of garnet and amphibole with an assumed average 95% CI for each measurement as ±30°C (Graham and Powell, 1984) (Amphibole and Garnet EPMA data can be found in Table S7 and S8 respectively; Analyses used for *T* calculations can be found in Table S9). **f**: Calculated using (Liao et al., 2021), standard measurement error is ±35°C, we assume

this is the maximum error **g**: Calculated using (Kohn and Spear, 1990) with an assumed *T* of 558°C and a maximum error of 0.1 GPa.

6. Discussion

6.1 Ages of metamorphism

Of the samples with sufficient U, all of which are garnet-epidote hornblendites, the following titanite dates were obtained (Figure 3): 148 ± 15 Ma (2se of lower concordia intercept; 21A1), 149.7± 8.7 Ma (2se of lower concordia intercept; 21C3), and 165 ± 17 Ma (2se of lower concordia intercept; 20E1). The dates are interpreted to be the timing of titanite growth in these rocks, as the closure temperature for U–Pb in titanite (≥800°C; Kohn, 2017; Holder et al., 2019), is estimated to be significantly higher than peak metamorphic temperatures (~550–600 °C, below). In these samples, titanite either exists as (hyp)idioblastic grains in apparent textural equilibrium with the other peak-metamorphic matrix minerals or as local coronae around rutile. In instances of the latter, the replacement of rutile is not associated with any other apparent reaction or retrogression of the surrounding matrix, suggesting that the replacement occurred near the metamorphic peak. From these observations, we interpret the titanite U–Pb dates to record near-peak metamorphism, possibly the earliest stages of decompression and cooling.

For one sample (21C3), a rutile date of 151.7 ± 3.8 Ma (2se of lower concordia intercept; Figure 3) was obtained. This is indistinguishable from the titanite dates of the same sample. The temperature range for partial retention of Pb in rutile is estimated to be ~550–650 °C, depending on the precise cooling history (Mezger et al., 1989; Cherniak, 2000; Vry and Baker, 2006; Kooijman et al., 2010; Smye et al., 2018). This is comparable to the estimates of peak metamorphic temperature (550–600°C, below), as recorded by the Zr-in-rutile thermometry

(Kohn, 2020). As such, we interpret the rutile date to record either the age of peak metamorphism or initial cooling immediately following peak metamorphism.

The Middle–Late Jurassic titanite and rutile dates are similar to dates reported for high-grade rocks (amphibolite to eclogite facies) in correlative subduction complexes along strike. Previous $^{39}Ar/^{40}Ar$ dates from (epidote) amphibolite-facies blocks on Cedros Island are of c. 170–160 Ma (Baldwin and Harrison, 1992). In the Franciscan Complex of California, $^{39}Ar/^{40}Ar$ (hornblende, white mica) and Lu–Hf (garnet) dates are broadly in the range of c. 170–155 Ma (Anczkiewicz et al., 2004; Wakabayashi and Dumitru, 2007; Shervais et al., 2011; Mulcahy et al., 2014; Rutte et al., 2020). Farther north, in the Easton metamorphic suite of Washington, c. 170–160 Ma $^{39}Ar/^{40}Ar$ hornblende and U–Pb titanite dates have also been reported (Cordova et al., 2019; Cunetta et al., 2025).

The agreement in the timing of high-grade metamorphism and subsequent exhumation over thousands of kilometers along the western coast of North America is consistent with fore-arc ophiolite ages (Shervais et al., 2004, 2005) and large-scale arc flare-ups (Ducea et al., 2015) which may signify a significant geodynamic event affecting the entirety of the active margin at the time.

6.2 Metamorphic temperatures

6.2.1 Peak metamorphism: Metamorphic temperatures calculated using Zr-in-rutile thermometry (Kohn, 2020; 530–636°C) agree well with estimates from the Fe–Mg garnet–hornblende exchange thermometer (garnet rims and matrix hornblende; Graham and Powell, 1984; ~500-670°C), and the Ti-in-amphibole thermometer (Liao et al., 2021; ~480–600°C). Given the

consistency among these results and lack of significant spatial variability of Zr-in-rutile temperatures (e.g., minimal variability within grains, no significant temperature differences between matrix grains vs inclusions in garnet, or any spatial temperature trends throughout the samples), we interpret the higher range of temperatures estimated from each sample to represent the peak metamorphic temperatures (e.g., Harvey et al., 2021), while the lower temperatures represent a prograde, near-peak temperature or a slight regression.

6.1.2 Apparent discrepancy of Zr-in-titanite temperatures: The temperatures calculated using the Zr-in-titanite thermometer are 100–200°C higher than the temperatures determined by the Zr-in-rutile thermometer, the Ti-in-amphibole thermometer, or the garnet-hornblende Fe–Mg exchange thermometer. As discussed with the U–Pb dates, above, titanite is texturally interpreted to be a near-peak-metamorphic mineral in local equilibrium with the other matrix minerals of the rock or as coronae around rutile, possibly associated with initial decompression or cooling following peak metamorphism. Considering these textural observations, as well as the general agreement of other thermometers, we do not consider the Zr-in-titanite temperatures to be accurate estimates of the temperatures reached by these rocks. The reasons for this discrepancy in temperature estimates could be thermodynamic or kinetic and are discussed further below.

6.3 Metamorphic pressures

6.3.1 Thermobarometric restrictions: Due to the lack of plagioclase in many of our samples, common thermobarometers for mafic rocks such as the garnet–plagioclase–hornblende–quartz geobarometer (GPHQ; Kohn and Spear, 1990), garnet–Al silicate–plagioclase geobarometer

(GASP; Ghent, 1976), or the titanite–zoisite/clinozoisite–anorthite–rutile–quartz geobarometer (TZARS; Kapp et al., 2009) could not be used. The pressures determined via QuiG for our garnet-hornblendites span a wide range (~0.7–1.7 GPa; Figure 4). Depending on how these values are interpreted, the pressure estimates range from mid-amphibolite facies to eclogite facies (Figure 5).

6.3.2 Interpreting QuiG datasets: There is not a standardized way to interpret QuiG results as every study is limited by factors such as sample sizes, rock types, tectonic environments, or specific geological or sample context. However, there are a few prevailing strategies. In some cases, the highest calculated P_{inc} (the stress on an inclusion) is taken to calculate P_{trap} (the pressure at which an inclusion was entrapped in a host; Kohn et al., 2023) (e.g., Spear et al., 2014, 2024; Wolfe et al., 2023), under the assumption that P_{inc} may be modified to lower pressure during decompression (for moderate- to high-pressure rocks in the alpha-quartz stability field) but should not generally be modified toward greater values. Such an approach requires that a sufficiently representative dataset has been collected to be confident one has captured the highest P_{inc}. In detail, this implicitly depends on the slope of the retrograde *P–T* path relative to the slopes of the isomekes. In cases where the retrograde path crosses isomekes toward higher P_{trap}, particularly from garnet growth approaching or within the beta-quartz stability field (e.g., Autrey et al., 2025), the opposite may be assumed, in which the lowest grouping of (even tensile) P_{inc} may be selected. Another approach has been to look at the average spectra shift of the analyses, particularly when the number of measurements is large and the distribution of measurements is small (e.g., Tuttle and Henry, 2023 in which $N > 200$ and P_{inc} range ~0.2 GPa). A similar technique is used in (Cisneros et al., 2022), where the P_{inc} data is averaged and then used to

calculate an average P_{trap}. Another technique used by (Harvey et al., 2021) is to combine all data to calculate a weighted mean, its uncertainty, and an MSWD, with statistical testing for the shape of the distribution and possibility of discrete and geologically significant sub-populations, representative of different conditions of growth or re-equilibration.

In each of these scenarios, a basic (sometimes implicit) assumption is that there should be a singular representative value for P_{trap} corresponding to a homogeneous stress distribution across the minerals in the rock (corresponding to lithostatic pressure). However, this assumption has been questioned. Synchrotron analyses of garnet grains showed residual stress heterogeneities ranging from 100 MPa to 1 GPa over scales of 10–100 μm (Jacob et al., 2025). These findings suggest that polycrystalline rocks may experience different deformation mechanisms spatially depending on local stresses. This implies there may be natural grain-scale scatter in unmodified P_{inc} relative to the lithostatic pressure, beyond the uncertainty of the measurements, on the order of several 100 MPa. In addition, particularly for environments with high rates of fluid production, such as subduction zones, it has been questioned whether a quasi-constant lithostatic pressure should be assumed. For example, Viete et al., (2018) observed Raman peak shifts among quartz grains in close proximity within eclogite-facies garnet corresponding to ~100–300 MPa pressure fluctuations; having no objective reason to select one pressure estimate over another, they interpreted the variation to reflect fluctuations in pore-fluid pressure in association with episodic fluid-production and migration (Viete et al., 2018). In aggregate, these observations suggest that the pressures retained in quartz inclusions might be affected simultaneously by pressure fluctuations during garnet growth and dissolution (Viete et al., 2018), local strains within the garnet due differences in elastic moduli and thermal expansivity between

the quartz and garnet, as well as localized stresses of minerals adjacent to or in contact with the host garnet (Jacob et al., 2025).

6.3.3 Interpretation of QuiG results: In the case of our samples, care was taken to (1) measure quartz inclusions within the same compositional zones of garnet (garnet mantles and rims to best correlate with temperature estimates of the matrix), (2) avoid fractures or proximity to other inclusions or proximity to the surface of the thin sections, and (3) measure quartz inclusions that are approximately equant. From these constraints, there is no objective observational reason to discard any of the measurements as less reliable than the others. If we were to take the highest *P* isomeke for each sample, our minimum estimated peak P_{trap}, across samples corresponds to eclogite facies: ~1.2–1.7 GPa (Figure 4,5). Eclogite (*sensu stricto*) blocks are known to exist on Cedros Island, however they have only been seen farther to the north, partially overprinted by blueschist-facies metamorphism (Baldwin and Harrison, 1992), but were not observed around Punta Prieta Ridge during our fieldwork. This finding would be of great interest because such hornblendite blocks are common in the area and may represent a greater prevalence of eclogite-facies metamorphism than otherwise assumed. However, if we were to take the approach of averaging the peak shifts of the analyses for each sample, the *P* range would be ~0.5 GPa lower: ~0.7–1.4 GPa (Figure 5). This *P* range is more consistent with (garnet–epidote) amphibolite facies, with only the upper end of *P* estimates bleeding into the eclogite facies. If we assume that the variation in pressure is associated with episodic garnet growth during fluid-over pressure events associated with local fluid production and migration (e.g., Viete et al., 2018), then the ambient, lithostatic pressure might more properly be estimated by the lowest P_{trap} ~0.7 GPa, corresponding strictly to amphibolite-facies conditions—with greater values representing the

magnitude of over-pressure excursions. Or if one considers that the range of values is due to grain-scale stress heterogeneity in the absence of fluid-overpressure (e.g., Jacobs et al., 2025), then the lithostatic pressure estimate would be somewhere in the range of the measured values: 0.7–1.7 GPa. If one were to grossly assume that these samples—owing to similarities of age, lithology, geographic and structural proximity, and temperature estimates—experienced the same metamorphic conditions, then broad agreement among the ranges of measured values across samples is suggestive of a pressure ~1 GPa (Figure 5). With these strategies for interpreting QuiG data and uncertainties in the measurement considered, we feel that the entire range of P_{trap} calculated for these samples should be reported. There is no objective reason to ignore any of our calculated pressures by picking the highest, lowest, or average P_{trap}.

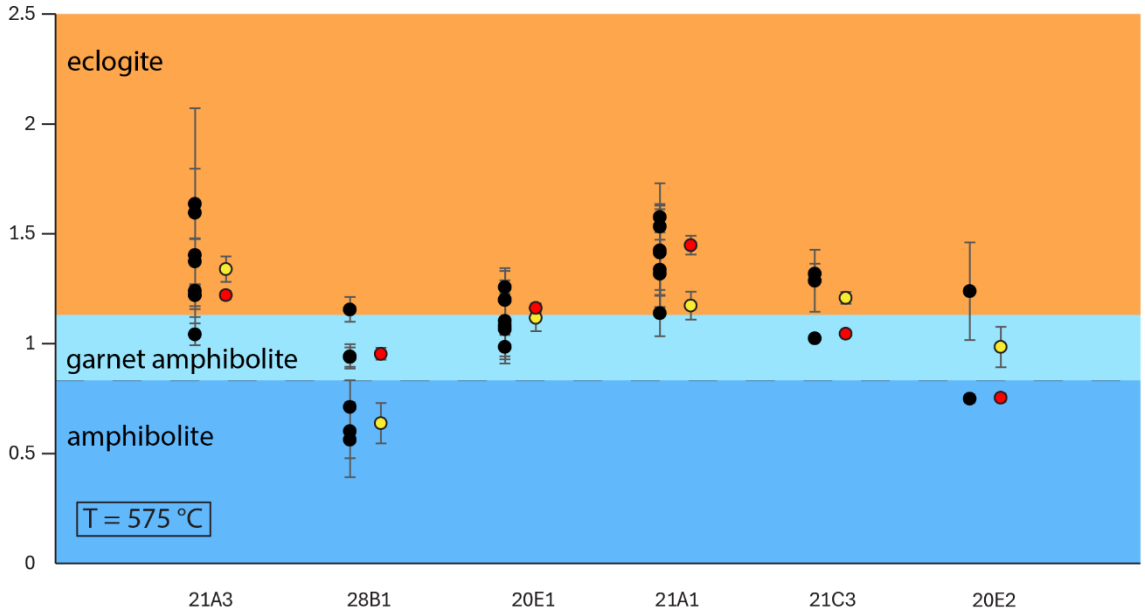


Figure 5: Maximum QuiG-derived pressures at 575°C. Points in black are pressures of individual inclusions, while points in yellow are the pressures derived from averaging the peak shifts of each inclusion and points in red are weighted mean averages of the pressures of the individual inclusions. Uncertainties are shown as 2se (abs). Approximate facies boundaries from (Hacker et al., 2003).

6.4 Estimate of subduction zone thermal structure

Choices in the interpretation of QuiG results have direct impact on the interpretation of the subduction-zone thermal structure in the Middle to Late Jurassic. Taking the upper range of pressure estimates (1.7 GPa), one calculates an apparent thermal gradient (thermobaric ratio) of ~350 °C/GPa, which is typical of *P–T* estimates from subduction-zone rocks globally (Kohn and Penniston-Dorland, 2017; Agard et al., 2018; Brown and Johnson, 2019). Taking the mean or lower range of pressure estimates, the calculated apparent thermal gradients are among the hottest reported for global subduction-zone environments, ~600–850 °C/GPa, comparable to estimates of metamorphic soles beneath ophiolites (e.g., Agard et al., 2018). It has been suggested that slab-top *T/P* is highest during subduction initiation (as recorded by metamorphic soles beneath fore-arc ophiolites, e.g., Agard et al., 2018) and lowers toward a steady-state over 10–30 Ma (e.g., Gerya et al., 2002; Van Keken et al., 2018; Holt and Condit, 2021; England and Smye, 2023; Epstein et al., 2024).

In the case of Baja California, the timing of subduction initiation is debated. Continuous "fast" tomographic anomalies traced into the lower mantle and paleomagnetic data have been used to suggest continued eastward subduction since the Triassic (Boschman et al., 2018). In this scenario, the Middle to Late Jurassic rocks of this study formed in a subduction zone that had been ongoing for at least several 10s of Ma and the lower estimates for *T/P* would be broadly consistent with expectations of a typical, mature subduction zone. However, if the higher end of the *T/P* estimates are accurate, then an alternative geodynamic scenario is required to explain

higher-than-average *T/P* in a "mature" subduction zone. Alternatively, it has been suggested from the correlative Franciscan Complex of California, that formation of a Middle to Late Jurassic fore-arc ophiolite in correlation with metamorphism and exhumation of high-grade blocks (amphibolite and eclogite; e.g., Rutte et al., 2020) are associated with terrane accretion and outboard re-initiation of subduction at that time (e.g., Schweickert, 2015). The uncertainty of the pressure estimates for these rocks therefore has significant consequences in regard to preferred models for the evolution of this active margin.

6.5 Kinetic and thermodynamic controls on Zr incorporation in titanite

6.5.1 One-to-one incorporation of Zr from reactant rutile: It has been shown (Lucassen et al., 2010; Cruz-Uribe et al., 2018; Page et al., 2023) that Zr-in-titanite temperatures tend to be anomalously high in titanite that grew at the expense of rutile. In these studies, the explanation given for these higher temperatures is a ~1:2.5 dilution of Zr into titanite when it replaces rutile. This apparent ~1:2.5 "dilution" is an effect of the greater molar mass of titanite, compared to rutile (~80 g/mol for pure rutile; ~197 g/mol for pure titanite). This difference in molar mass means that 1g of Zr corresponds to a ~2.5x higher concentration (µg Zr/ g mineral) in rutile as opposed to the same 1 g of Zr in titanite. Rutile takes up Zr^{+4} by replacing Ti^{+4} in its octahedral site; in the hypothesis of direct replacement of rutile by titanite, the Zr^{+4} and Ti^{+4} are transferred 1:1 into titanite's octahedral site. In other words, the growth of titanite from rutile is a closed system with respect to Zr and Ti, resulting in an equal Zr/Ti ratio in reactant rutile and product titanite. The molar volume difference between the two minerals means that as titanite grows at the expense of rutile, it will take up more space, growing both inward (replacing rutile) and outward toward the matrix (this matter is discussed in more detail below).

While many of the Zr concentrations measured correspond with the ~1:2.5 signal, there are a minority of measured concentrations above this signal value and many below (Figure 6). In three samples (21A1, 20G1, and 21C3), the distribution of Zr in titanite measurements agrees well with the distribution of measured Zr in rutile (Zr in titanite ≈ Zr in rutile•0.4). In four other samples, (28A1, 20E1, 20E3, 21A2), Zr-in-titanite measurements overlap with Zr-in-rutile measurements at the 1:2.5 scaling, but the mode of data skew toward lower concentrations, approaching, but not quite reaching predicted equilibrium concentrations for growth at near-peak *P–T* (assuming *T* = Zr-in-rutile *T*; *P* = 1 GPa, $a_{TiO2} = a_{SiO2} = 1$). There are also a minority of measurements of Zr in titanite that skew toward significantly higher values than expected for the 1:2.5 ratio.

Sample 20E1 is a particularly illustrative example, because the titanite grains are quite large, allowing the spatial variability of the Zr measurements to be considered (Figure 7). In this sample, there is a minor mode of data (~45 μg/g), corresponding to titanite cores, which matches well with well to the 1:2.5 ratio of Zr in rutile. A second mode at lower concentration (~15-20 μg/g) is spatially associated with the mantles and rims. As a hypothesis, we suggest this pattern could be explained by initial titanite growth and inward replacement of rutile recording the ~1:2.5 ratio expected for closed system transfer of Ti and Zr from rutile to titanite in the titanite core. In contrast, the outward (toward matrix) growth of titanite is characterized by lower incorporation of Zr, trending toward a concentration of plausible equilibrium with the matrix. The extent to which equilibrium was actually reached is considered in the next section. Due to negligibly low diffusivity of Zr in titanite at these temperatures (Holder et al., 2019), diffusive re-equilibration following growth would not be expected, preserving the heterogeneous and anomalously high Zr concentrations across the grains. The highest concentrations of Zr in

titanite, greatly exceeding the expected 1:2.5 ratio, also come from the titanite core. These are a minority of the data and could reflect growth from rutile (now consumed) with even higher Zr concentration, small unrecognized inclusions of rutile or zircon caught in the ablations, or a crystallographic effect such as sector zoning (Hayden et al., 2008; Kohn, 2017; Cherniak 2000).

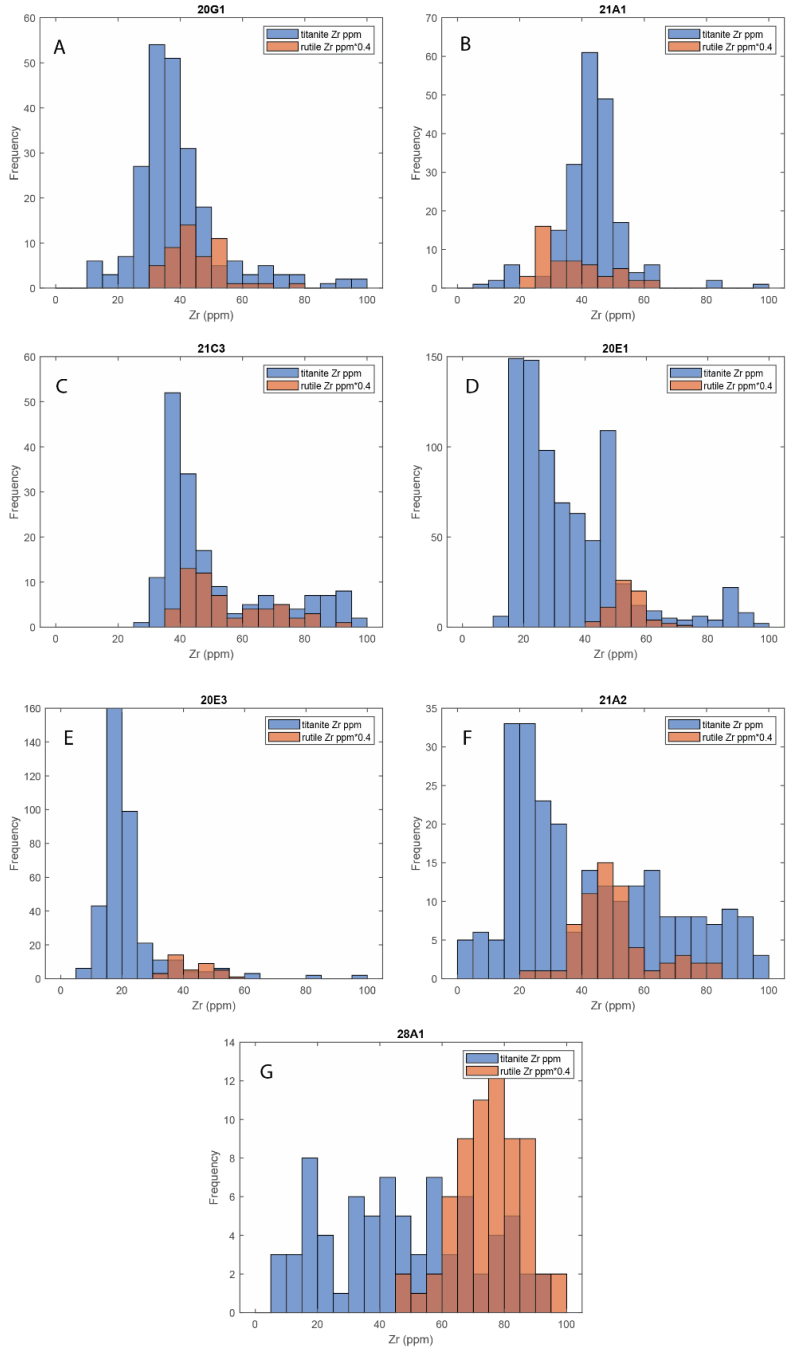
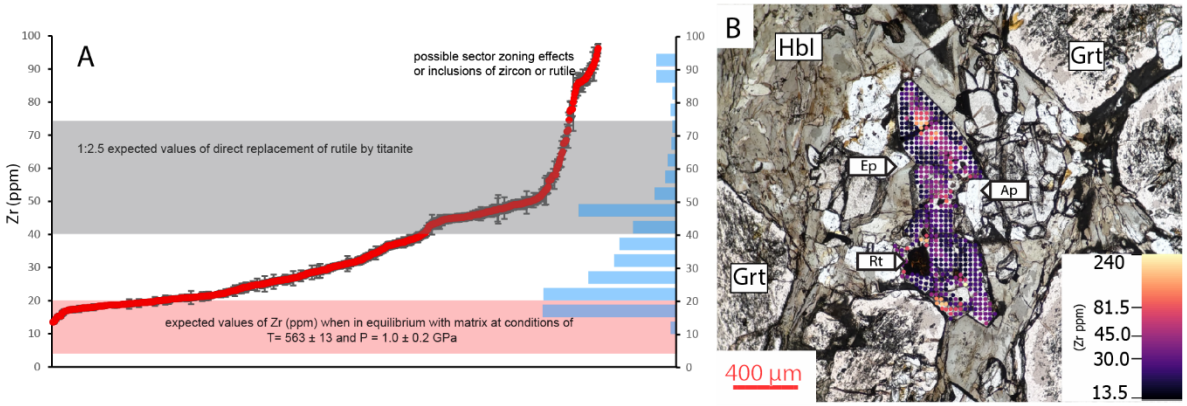


Figure 6: In samples (A) 20G1, (B) 21A1, and (C) 21C3 the distribution of Zr in titanite measurements agrees well with the distribution of Zr in rutile as expected for direct replacement of rutile by titanite in closed system with respect to Ti and Zr (Zr in titanite ≈ Zr in rutile•0.4). In samples (D) 20E1, (E) 20E3, (F) 21A2, and (G) 28A1, Zr in titanite measurements agree with the measurements of Zr in rutile (1:2.5), but a majority of the data skews toward lower concentrations—possibly reflecting a trend toward matrix equilibrium—and a minority skew toward higher concentrations. See text for discussion.

Figure 7: A) Rank-order plot and histogram of Zr in titanite from sample 20E1, showing modes of data at ~45 and



~20 µg/g. B) Photomicrograph of a relatively large titanite grain, annotated with spot locations colored by their Zr content (log-scale color gradient) and illustrating the spatial distribution of the measured data. The 45 µg/g mode corresponds to titanite cores and is consistent with the expected ~1:2.5 dilution ratio for direct replacement of rutile by titanite. The ~20 µg/g mode corresponds to the rim is consistent with equilibrium Zr concentrations at near-peak *P–T*, but with a_{TiO2} and a_{SiO2} <1 (Figure 8). The overall pattern of data is consistent with initial disequilibrium growth of titanite on rutile (direct 1:1 incorporation of Zr into the Ti site from reactant rutile), with continued growth toward the matrix approaching plausible local equilibrium, albeit with a_{TiO2} << 1 due to consumption (or shielding) of rutile and a_{SiO2} < 1 due to limited grain-boundary diffusivity. See text for discussion.

6.5.2 Uncertainties in thermodynamic equilibrium: The equation for the concentration of Zr in titanite derived from (Hayden et al., 2008) is:

(3)

Here, as before, we take sample 20E1 as an example, because of the spatial context provided by its larger titanite grains, but comparable calculations could be conducted for any of the other samples with similar results. If we assume T = 563 °C (Zr-in-rutile T) and P = 1 GPa (QuiG ~0.8–1.2 GPa for this sample) and $a_{SiO2} = a_{TiO2} = 1$, reflecting the presence of minor quartz and rutile in the sample, the predicted Zr concentration in titanite from Equation 1 is 1.3 μg/g. This is an order-of-magnitude lower than our lowest measured Zr concentration in this sample's titanite rim (13.7 μg/g). Given that the observed mineralogy and other thermometry does not permit substantially higher T, we consider the effects of P and $a_{SiO2} \bullet a_{TiO2}$ on the expected concentrations. For 13.7 μg/g Zr in titanite, at equivalent near-peak T and $a_{SiO2} = a_{TiO2} = 1$, P would need to have been ≲ 0.3 GPa. This low P and high T (~62°C/km) does not correspond with a reasonable geothermal gradient (~10–20°C/km) we would expect to see in even a hot subduction zone setting. If one considers that pressure may have been higher, the discrepancy between prediction and observation becomes greater, with higher pressure favoring still lower Zr in titanite.

Another consideration is that the thermobarometer as described by Equation (3) is strongly controlled by the activities of TiO_2 and SiO_2, with lower activities of either contributing to greater incorporation of Zr in titanite. Assuming equilibrium was reached, and one knows the *P–T* conditions of titanite growth, one can calculate the activity product (a_{SiO2}•a_{TiO2}) corresponding to a given Zr concentration. Using a Monte Carlo simulation where $T = 563 \pm 13$°C (2se Gaussian distribution; assuming near-peak *T* titanite growth from Zr-in-rutile *T*), $P = 0.8–1.2$ GPa (uniform distribution; reflecting the range of observed QuiG *P*), and the observed lowest rim concentration of Zr = 13.7 μg/g, the activity product a_{SiO2}•$a_{TiO2} = 0.1040$, 95% CI [0.0483, 0.2207] (Figure 8). This means that the observed Zr in titanite concentrations could be explained as equilibrium concentrations reflective of near-peak *P–T* growth, but with a_{SiO2} and a_{TiO2} substantially less than unity. Alternatively, one could predict a range of expected equilibrium Zr-in-titanite concentrations as a function of uncertainty in a_{SiO2} and a_{TiO2}. For example, taking again $T = 563 \pm 13$°C (2se; Gaussian distribution), $P = 0.8–1.2$ GPa (uniform distribution), and considering both a_{SiO2} and a_{TiO2} to range anywhere from 0.2–1.0 (uniform distribution), results in Zr concentrations = 4.5, 95% CI [1.2, 22.4] μg/g (Figure 9), which is well within agreement of the lower mode of titanite rim data (~15–20 μg/g). As above, assuming lower pressure (titanite growth during decompression from peak *P*) favors higher Zr in titanite, or higher $a_{SiO2}.a_{TiO2}$ at equivalent Zr in titanite. Together, these analyses indicate that it may be both a slight change in *P* and significant decreases in the activities of silica and titania that explain the abundance of Zr concentrations in titanite less than expected for the 1:2.5 ratio of rutile replacement, but greater than the expected matrix equilibrium from assumed $a_{SiO2} = a_{TiO2} = 1$. From this perspective, the best practice in application of Zr-in-titanite thermometry to such rocks may be to take the minimum measured Zr concentration as an upper bound for peak *P–T*. Interestingly, this

approach would be the direct opposite of Zr-in-rutile thermometry, for which it is common practice to look at the rutile with the highest concentration of Zr as the nearest estimate of peak *T* (Harvey et al., 2021).

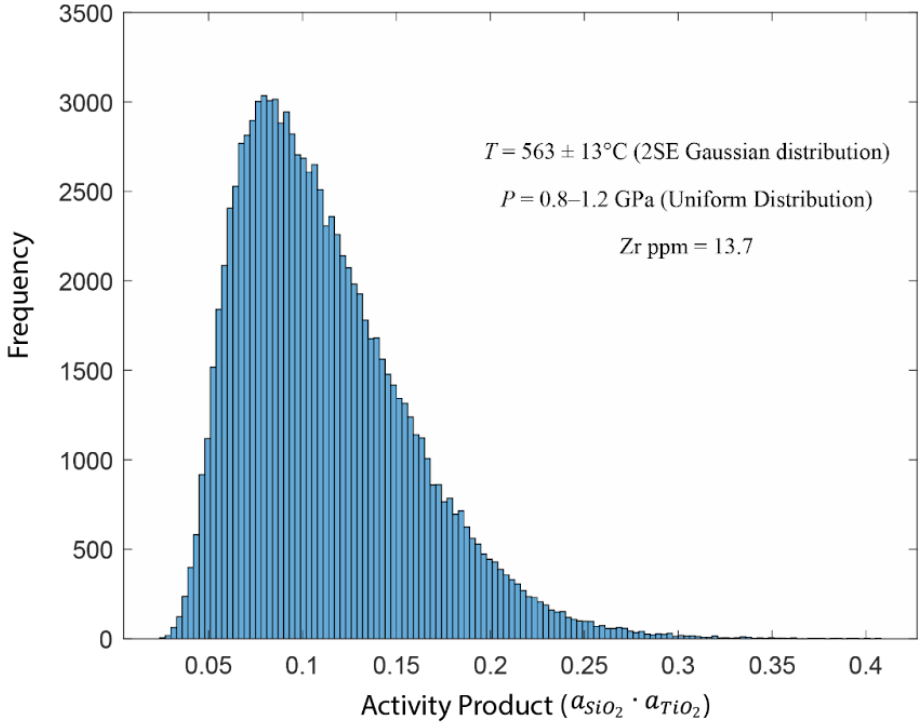


Figure 8: The lowest measured Zr in titanite is consistent with near-peak *P–T* titanite growth at a_{TiO2} a_{SiO2} << 1. Monte-Carlo simulation of activity product (a_{TiO2} a_{SiO2}) from Equation X, for growth of titanite rims in sample 20E1, using the lowest measured Zr in titanite concentration. The distribution corresponds to a range of permissible values in accordance with reported uncertainties in the coefficients of the Zr-in-titanite thermometer (Hayden et al., 2008; assumed to be Gaussian), uncertainties in Zr-in-rutile temperature (Figure 2; Table 4; Gaussian), and the range of QuiG pressures (Figure 4; Table 4; uniform). See text for discussion.

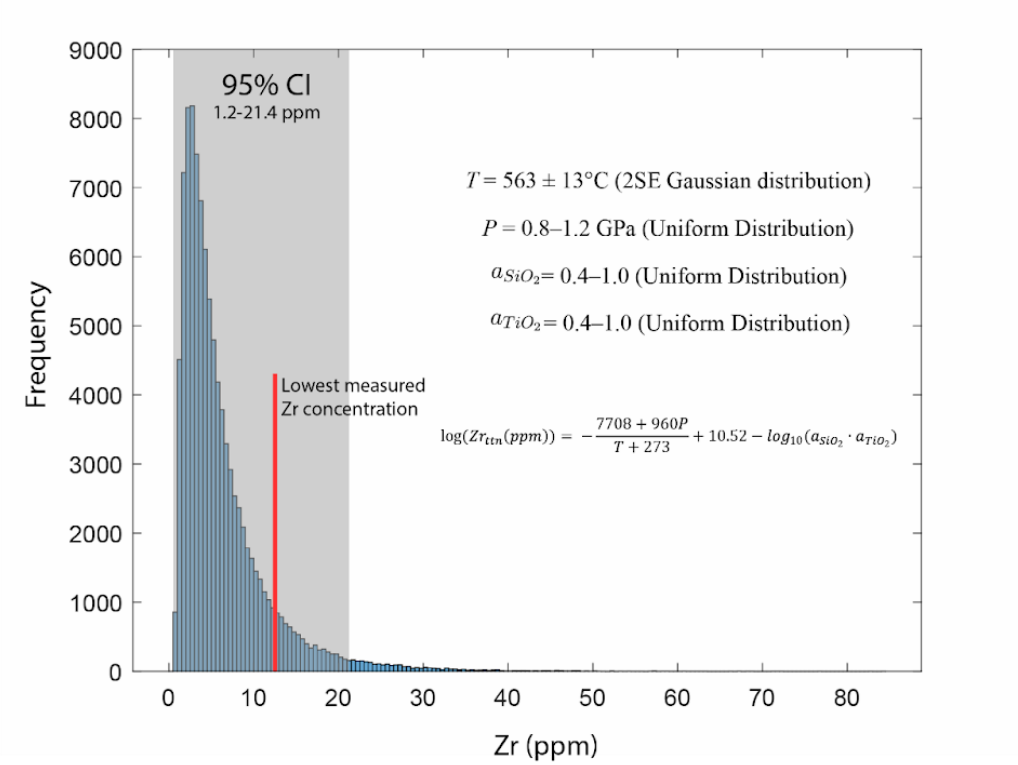


Figure 9. Uncertainty in a_{TiO2} and a_{SiO2} causes substantial uncertainty (and upward skewing) of expected concentrations of Zr in titanite. Monte-Carlo simulation of Zr in titanite concentrations for sample 20E1 from Equation X, at near-peak *P–T* conditions and a range of a_{TiO2} and a_{SiO2} between 0.4 and 1. Values of $a_{TiO2} < 1$ may be expected for titanite rim growth due to consumption rutile (or shielding of relict rutile in titanite interiors). Values of $a_{SiO2} < 1$ may be expected along the rutile–titanite interface, an oxide boundary shielded from the matrix. Values of $a_{SiO2} < 1$ may also be expected along titanite rims owing to limited grain-boundary diffusivity during retrogression. The plotted distribution corresponds to a range of permissible values in accordance with uncertainties in the coefficients of the Zr-in-titanite thermometer (Hayden et al., 2008; assumed to be Gaussian), Zr-in-rutile temperature (Figure 2; Table 4; Gaussian), QuiG pressures (Figure 4; Table 4; uniform), as well as a_{TiO2} and a_{SiO2} (0.4–1.0;

uniform). The low-Zr mode of measurements from sample 20E1 (~15–20 μg/g; Figure 7) falls within the 95% confidence interval of simulated values.

6.5.3 Potential controls on the decrease of activity product: As mentioned in the previous section, variations in the activities of SiO_2 and TiO_2, and to a lesser degree *P* can contribute to substantially higher equilibrium Zr concentrations in titanite. The logical question is then, which chemical processes can cause this drastic change in activities during titanite growth? Especially considering, at the time of rutile growth, it seems reasonable to assume that $a_{SiO2} = 1$ (also impacts the Zr-in-rutile thermometer), as our rutile yielded temperature estimates in reasonable agreement with matrix amphibole and garnet (Fe–Mg garnet-hornblende and Ti-in-amphibole thermometry; Figure 2). This suggests a change from prograde to peak metamorphism, during which rutile is interpreted to have grown and the early stages of retrogression in which titanite is interpreted to have formed. One consideration is that prograde metamorphism was likely characterized by the presence (and production) of a free fluid. The presence of this fluid can allow for more efficient intragranular transport of Si, Ti, and Zr, facilitating equilibrium among quartz, zircon, and rutile. However, if titanite is growing during retrograde metamorphism, hydrous fluids along grain boundaries of minerals should be reduced (e.g., Kohn et al., 2016). The intergranular transport of elements could be significantly hindered by the lack of such a fluid in the matrix, an interpretation consistent with the often coronal relationship of titanite around rutile.

As mentioned above, titanite has greater molar mass than rutile, meaning it must grow both toward and away from the rutile that it is replacing during coronal replacement (Figure 10). This means that there are two growth interfaces for the titanite, one in contact with the rutile and

one in contact with the surrounding matrix. These two interfaces may experience vastly different chemical conditions. At the titanite–rutile interface a_{TiO2} is likely at or near unity, but a_{SiO2} will be significantly lower reflecting the oxide interface along which the reaction is occurring. At the outer growth interface, titanite is shielded from the interior rutile, resulting in $a_{TiO2} < 1$, reflecting the lack of rutile in the matrix adjacent to the growing titanite (e.g., Kapp et al., 2009; Corrie et al., 2010; Ashley and Law, 2015). The extent to which $a_{SiO2} < 1$ depends on the proximity of quartz in the matrix and grain-boundary diffusivity of Si (e.g., Kohn et al., 2016). In other words, $a_{SiO2} \bullet a_{TiO2}$ should be expected to be less than unity and exhibit high spatial variability during direct replacement of rutile by titanite. The combination of decreased intergranular elemental transport and decreased activities of silica and titania at both the growth interfaces of titanite during the replacement of rutile may be the factors that cause these anomalously high Zr concentrations in titanite.

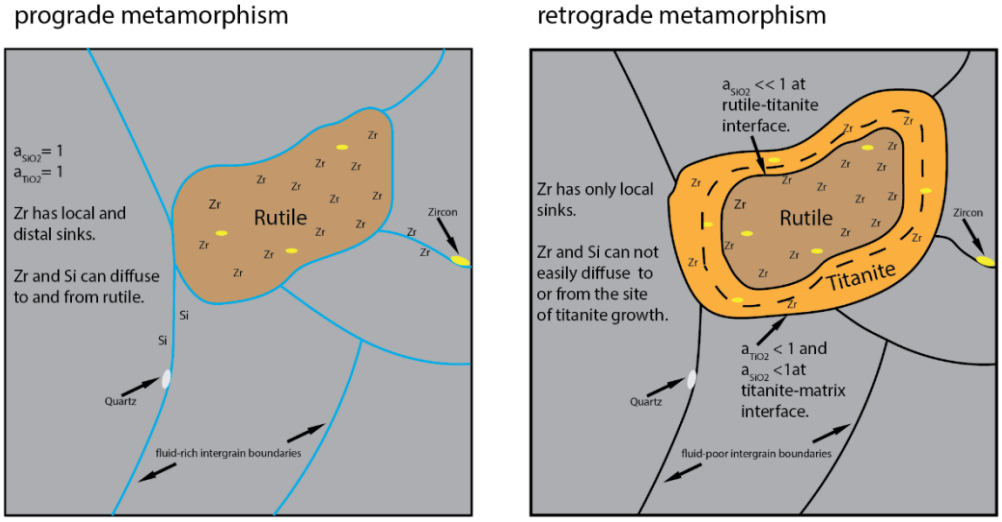


Figure 10. During prograde metamorphism, fluid-rich grain boundaries facilitate equilibration of rutile with trace zircon and quartz in the matrix; Zr in rutile temperatures calculated with $a_{SiO2} = 1$ reliably record peak *T*, in agreement with Fe–Mg garnet hornblende and Ti-in-amphibole thermometry. During initial retrogression, consumption of grain-boundary fluid limits intragranular elemental transport limited elemental transport is indicated by coronal relationship of titanite on rutile. Initial growth of titanite characterized by direct (disequilibrium) incorporation of Zr from reactant rutile (~1:2.5 µg/g ratio). Continued inward growth, along the rutile–titanite boundary is limited by elemental transport through the coronal titanite and likely characterized by $a_{SiO2} << 1$. Continued outward growth is characterized by $a_{TiO2} < 1$, due to shielding of the reactant rutile from the outer titanite grain boundary and $a_{SiO2} < 1$, due to limited grain-boundary diffusivity.

7. Summary and Implications

The results of thermobarometry show that these samples likely experienced amphibolite to eclogite facies metamorphism (P of ~0.7–1.7 GPa; T of ~500–630°C). The subduction zone that created these blocks may have experienced geothermal gradients ranging from ~350°C/GPa (typical of subduction zones) to ~600–850°C/GPa (typical of metamorphic soles), depending on the strategy one employs for the interpretation of QuiG barometry. QuiG barometry can be helpful in determining P that is experienced by rocks independent of assumptions regarding chemical equilibrium. However, QuiG datasets, as shown here, often exhibit considerable scatter; baric interpretation depends heavily on how one resolves such scatter. Calculated Zr-in-titanite temperatures were anomalously high, likely associated with kinetic and thermodynamic effects of direct replacement of rutile in a fluid-undersaturated environment that limited intragranular diffusivity of Zr, Ti, and Si. These results imply that it may be best to extensively analyze titanite and look to the lowest temperatures calculated if they are otherwise anomalously high, and titanite grows at the expense of rutile.

Bibliography

Agard, P., Plunder, A., Angiboust, S., Bonnet, G., and Ruh, J., 2018, The subduction plate interface: rock record and mechanical coupling (from long to short timescales): Lithos, v. 320–321, p. 537–566, doi:10.1016/j.lithos.2018.09.029.

Anczkiewicz, R., Platt, J.P., Thirlwall, M.F., and Wakabayashi, J., 2004, Franciscan subduction off to a slow start: evidence from high-precision Lu–Hf garnet ages on high grade-blocks: Earth and Planetary Science Letters, v. 225, p. 147–161, doi:10.1016/j.epsl.2004.06.003.

Angel, R.J., Murri, M., Mihailova, B., and Alvaro, M., 2019, Stress, strain and Raman shifts: Zeitschrift für Kristallographie - Crystalline Materials, v. 234, p. 129–140, doi:10.1515/zkri-2018-2112.

Ashley, K.T., and Law, R.D., 2015, Modeling prograde TiO2 activity and its significance for Ti-in-quartz thermobarometry of pelitic metamorphic rocks: Contributions to Mineralogy and Petrology, v. 169, p. 23, doi:10.1007/s00410-015-1118-7.

Autrey, S., Bonamici, C., and Williams, M.L., 2025, Applications of Quartz in Garnet Elastic Geobarometry to Mid Crustal Barrovian Metamorphic Rocks Demonstrated Using Tensionally Stressed Inclusions From the Grand Canyon: Journal of Metamorphic Geology, v. 43, p. 734–753, doi:10.1111/jmg.70002.

Baldwin, S.L., and Harrison, T.M., 1992, The P-T-t history of blocks in serpentinite-matrix mélange, west-central Baja California: Geological Society of America Bulletin, v. 104, p. 18–31, doi:10.1130/0016-7606(1992)104%3C0018:TPTTHO%3E2.3.CO;2.

Brown, M., and Johnson, T., 2019, Metamorphism and the evolution of subduction on Earth: American Mineralogist, v. 104, p. 1065–1082, doi:10.2138/am-2019-6956.

Busby, C., Smith, D., Morris, W., and Fackler-Adams, B., 1998, Evolutionary model for convergent margins facing large ocean basins: Mesozoic Baja California, Mexico: Geology, v. 26, p. 227, doi:10.1130/0091-7613(1998)026%3C0227:EMFCMF%3E2.3.CO;2.

Cherniak, D.J., 2000, Pb diffusion in rutile: Contributions to Mineralogy and Petrology, v. 139, p. 198–207, doi:10.1007/PL00007671.

Cisneros, M., Behr, W.M., Platt, J.P., and Anczkiewicz, R., 2022, Quartz-in-garnet barometry constraints on formation pressures of eclogites from the Franciscan Complex, California: Contributions to Mineralogy and Petrology, v. 177, p. 12, doi:10.1007/s00410-021-01876-4.

Cizina, M.F., Mikesell, T.D., and Kohn, M.J., 2023, Optimizing Raman spectral collection for quartz and zircon crystals for elastic thermobarometry: American Mineralogist: Journal of Earth and Planetary Materials, v. 108, p. 915–927, doi:10.2138/am-2022-8423.

Cordova, J.L., Mulcahy, S.R., Schermer, E.R., and Webb, L.E., 2019, Subduction initiation and early evolution of the Easton metamorphic suite, northwest Cascades, Washington: Lithosphere, v. 11, p. 44–58, doi:10.1130/L1009.1.

Corrie, S.L., Kohn, M.J., and Vervoort, J.D., 2010, Young eclogite from the Greater Himalayan Sequence, Arun Valley, eastern Nepal: P–T–t path and tectonic implications: Earth and Planetary Science Letters, v. 289, p. 406–416, doi:10.1016/j.epsl.2009.11.029.

Cruz-Uribe, A.M., Feineman, M.D., Zack, T., and Jacob, D.E., 2018, Assessing trace element (dis)equilibrium and the application of single element thermometers in metamorphic rocks: Lithos, v. 314–315, p. 1–15, doi:10.1016/j.lithos.2018.05.007.

Cunetta, N.S., Mulcahy, S.R., Schermer, E.R., and Smit, M.A., 2025, Early Jurassic subduction initiation recorded in the Easton metamorphic suite, Northwest Cascades (Washington, USA): Geological Society of America Bulletin, v. 137, p. 4431–4450, doi:10.1130/B38167.1.

Donovan, J.J., Lowers, H.A., and Rusk, B.G., 2011, Improved electron probe microanalysis of trace elements in quartz: American Mineralogist, v. 96, p. 274–282, doi:10.2138/am.2011.3631.

Donovan, J.J., Singer, J.W., and Armstrong, J.T., 2016, A new EPMA method for fast trace element analysis in simple matrices: American Mineralogist, v. 101, p. 1839–1853, doi:10.2138/am-2016-5628.

Ducea, M.N., Paterson, S.R., and DeCelles, P.G., 2015, High-Volume Magmatic Events in Subduction Systems: Elements, v. 11, p. 99–104, doi:10.2113/gselements.11.2.99.

Enami, M., Nishiyama, T., and Mouri, T., 2007, Laser Raman microspectrometry of metamorphic quartz: A simple method for comparison of metamorphic pressures: American Mineralogist, v. 92, p. 1303–1315, doi:10.2138/am.2007.2438.

England, P.C., and Smye, A.J., 2023, Metamorphism and Deformation on Subduction Interfaces: 1. Physical Framework: Geochemistry, Geophysics, Geosystems, v. 24, p. e2022GC010644, doi:10.1029/2022GC010644.

Epstein, G.S., Condit, C.B., Stoner, R.K., Holt, A.F., and Guevara, V.E., 2024, Evolving Subduction Zone Thermal Structure Drives Extensive Forearc Mantle Wedge Hydration: AGU Advances, v. 5, p. e2023AV001121, doi:10.1029/2023AV001121.

Ferry, J.M., and Watson, E.B., 2007, New thermodynamic models and revised calibrations for the Ti-in-zircon and Zr-in-rutile thermometers: Contributions to Mineralogy and Petrology, v. 154, p. 429–437, doi:10.1007/s00410-007-0201-0.

Gerya, T.V., Stöckhert, B., and Perchuk, A.L., 2002, Exhumation of high pressure metamorphic rocks in a subduction channel: A numerical simulation: Tectonics, v. 21, doi:10.1029/2002TC001406.

Gheni, E.D. Plagioclase-garnet-Al2SiOr-quartz:.s potential geobarometer-geothermometer:

Graham, C.M., and Powell, R., 1984, A garnet–hornblende geothermometer: calibration, testing, and application to the Pelona Schist, Southern California: Journal of Metamorphic Geology, v. 2, p. 13–31, doi:10.1111/j.1525-1314.1984.tb00282.x.

Hacker, B.R., Abers, G.A., and Peacock, S.M., 2003, Subduction factory 1. Theoretical mineralogy, densities, seismic wave speeds, and H_2 O contents: Journal of Geophysical Research: Solid Earth, v. 108, p. 2001JB001127, doi:10.1029/2001JB001127.

Harvey, K.M., Penniston Dorland, S.C., Kohn, M.J., and Piccoli, P.M., 2021, Assessing *P T* variability in mélange blocks from the Catalina Schist: Is there differential movement at the subduction interface? Journal of Metamorphic Geology, v. 39, p. 271–295, doi:10.1111/jmg.12571.

Hayden, L.A., Watson, E.B., and Wark, D.A., 2008, A thermobarometer for sphene (titanite): Contributions to Mineralogy and Petrology, v. 155, p. 529–540, doi:10.1007/s00410-007-0256-y.

Holder, R.M., Hacker, B.R., Seward, G.G.E., and Kylander-Clark, A.R.C., 2019, Interpreting titanite U–Pb dates and Zr thermobarometry in high-grade rocks: empirical constraints on elemental diffusivities of Pb, Al, Fe, Zr, Nb, and Ce: Contributions to Mineralogy and Petrology, v. 174, p. 42, doi:10.1007/s00410-019-1578-2.

Holt, A.F., and Condit, C.B., 2021, Slab Temperature Evolution Over the Lifetime of a Subduction Zone: Geochemistry, Geophysics, Geosystems, v. 22, p. e2020GC009476, doi:10.1029/2020GC009476.

Horton, F., Hacker, B., Kylander Clark, A., Holder, R., and Jöns, N., 2016, Focused radiogenic heating of middle crust caused ultrahigh temperatures in southern Madagascar: Tectonics, v. 35, p. 293–314, doi:10.1002/2015TC004040.

Izraeli, E.S., Harris, J.W., and Navon, O., 1999, Raman barometry of diamond formation: Earth and Planetary Science Letters, v. 173, p. 351–360, doi:10.1016/S0012-821X(99)00235-6.

Jacob, J., Van Schrojenstein Lantman, H., Cordonnier, B., Menegon, L., Wright, J., and Renard, F., 2025, Exhumation-induced residual stress in undeformed, ultra-high-pressure metamorphic rock:, doi:10.5194/egusphere-egu25-3540.

Jiao, S., Guo, J., Mao, Q., and Zhao, R., 2011, Application of Zr-in-rutile thermometry: a case study from ultrahigh-temperature granulites of the Khondalite belt, North China Craton: Contributions to Mineralogy and Petrology, v. 162, p. 379–393, doi:10.1007/s00410-010-0602-3.

Johnson, T.A., Cottle, J.M., and Larson, K.P., 2021, Delineation of multiple metamorphic events in the Himalayan Kathmandu Complex, central Nepal: Journal of Metamorphic Geology, v. 39, p. 443–472, doi:10.1111/jmg.12583.

Kapp, P., Manning, C.E., and Tropper, P., 2009, Phase equilibrium constraints on titanite and rutile activities in mafic epidote amphibolites and geobarometry using titanite–rutile equilibria: Journal of Metamorphic Geology, v. 27, p. 509–521, doi:10.1111/j.1525-1314.2009.00836.x.

Kimbrough, D.L. Tectonostratigraphic Terranes of the Vizcaino Peninsula and Cedros and San Benito Islands, Baja California, Mexico:

Kimbrough, D.L., and Moore, T.E., 2003, Ophiolite and volcanic arc assemblages on the Vizcaino Peninsula and Cedros Island, Baja California Sur, México: Mesozoic forearc lithosphere of the Cordilleran magmatic arc, *in* Tectonic evolution of northwestern Mexico and the Southwestern USA, Geological Society of America, doi:10.1130/0-8137-2374-4.43.

Kohn, M.J., 2020, A refined zirconium-in-rutile thermometer: American Mineralogist, v. 105, p. 963–971, doi:10.2138/am-2020-7091.

Kohn, M.J., 2014, “Thermoba-Raman-try”: Calibration of spectroscopic barometers and thermometers for mineral inclusions: Earth and Planetary Science Letters, v. 388, p. 187–196, doi:10.1016/j.epsl.2013.11.054.

Kohn, M.J., 2017, Titanite Petrochronology: Reviews in Mineralogy and Geochemistry, v. 83, p. 419–441, doi:10.2138/rmg.2017.83.13.

Kohn, M.J., and Corrie, S.L., 2011, Preserved Zr-temperatures and U–Pb ages in high-grade metamorphic titanite: Evidence for a static hot channel in the Himalayan orogen: Earth and Planetary Science Letters, v. 311, p. 136–143, doi:10.1016/j.epsl.2011.09.008.

Kohn, M.J., Mazzucchelli, M.L., and Alvaro, M., 2023, Elastic Thermobarometry: Annual Review of Earth and Planetary Sciences, v. 51, p. 331–366, doi:10.1146/annurev-earth-031621-112720.

Kohn, M.J., and Penniston-Dorland, S.C., 2017, Diffusion: Obstacles and Opportunities in Petrochronology: Reviews in Mineralogy and Geochemistry, v. 83, p. 103–152, doi:10.2138/rmg.2017.83.4.

Kohn, M.J., Penniston-Dorland, S.C., and Ferreira, J.C.S., 2016, Implications of near-rim compositional zoning in rutile for geothermometry, geospeedometry, and trace element

equilibration: Contributions to Mineralogy and Petrology, v. 171, p. 78, doi:10.1007/s00410-016-1285-1.

Kohn, M.J., and Spear, F.S., 1990, Two new geobarometers for garnet amphibolites with applications to southeastern Vermont: American Mineralogist, v. 75.

Kooijman, E., Mezger, K., and Berndt, J., 2010, Constraints on the U–Pb systematics of metamorphic rutile from in situ LA-ICP-MS analysis: Earth and Planetary Science Letters, v. 293, p. 321–330, doi:10.1016/j.epsl.2010.02.047.

Kylander-Clark, A.R.C., 2017, Petrochronology by Laser-Ablation Inductively Coupled Plasma Mass Spectrometry: Reviews in Mineralogy and Geochemistry, v. 83, p. 183–198, doi:10.2138/rmg.2017.83.6.

Kylander-Clark, A.R.C., Hacker, B.R., and Cottle, J.M., 2013, Laser-ablation split-stream ICP petrochronology: Chemical Geology, v. 345, p. 99–112, doi:10.1016/j.chemgeo.2013.02.019.

Liao, Y., Wei, C., and Rehman, H.U., 2021, Titanium in calcium amphibole: Behavior and thermometry: American Mineralogist, v. 106, p. 180–191, doi:10.2138/am-2020-7409.

Lucassen, F., Dulski, P., Abart, R., Franz, G., Rhede, D., and Romer, R.L., 2010, Redistribution of HFSE elements during rutile replacement by titanite: Contributions to Mineralogy and Petrology, v. 160, p. 279–295, doi:10.1007/s00410-009-0477-3.

Mazzucchelli, M.L., Angel, R.J., and Alvaro, M., 2021, EntraPT: An online platform for elastic geothermobarometry: American Mineralogist, v. 106, p. 830–837, doi:10.2138/am-2021-7693CCBYNCND.

Mezger, K., Hanson, G.N., and Bohlen, S.R., 1989, High-precision UPb ages of metamorphic rutile: application to the cooling history of high-grade terranes: Earth and Planetary Science Letters, v. 96, p. 106–118, doi:10.1016/0012-821X(89)90126-X.

Mulcahy, S.R., Vervoort, J.D., and Renne, P.R., 2014, Dating subduction zone metamorphism with combined garnet and lawsonite Lu–Hf geochronology: Journal of Metamorphic Geology, v. 32, p. 515–533, doi:10.1111/jmg.12092.

Page, F.Z., Storey, C.D., and EIMF, 2023, A rutile and titanite record of subduction fluids: Integrated oxygen isotope and trace element analyses in Franciscan high pressure rocks: Journal of Metamorphic Geology, v. 41, p. 767–786, doi:10.1111/jmg.12717.

Penniston-Dorland, S.C., Kohn, M.J., and Piccoli, P.M., 2018, A mélange of subduction temperatures: Evidence from Zr-in-rutile thermometry for strengthening of the subduction interface: Earth and Planetary Science Letters, v. 482, p. 525–535, doi:10.1016/j.epsl.2017.11.005.

Rutte, D., Garber, J., Kylander Clark, A., and Renne, P.R., 2020, An Exhumation Pulse From the Nascent Franciscan Subduction Zone (California, USA): Tectonics, v. 39, p. e2020TC006305, doi:10.1029/2020TC006305.

Schweickert, R.A., 2015, Jurassic evolution of the Western Sierra Nevada metamorphic province, *in* Geological Society of America Special Papers, Geological Society of America, v. 513, p. 299–358, doi:10.1130/2015.2513(08).

Sedlock, R.L., 1999, Evaluation of exhumation mechanisms for coherent blueschists in western Baja California, Mexico: Geological Society, London, Special Publications, v. 154, p. 29–54, doi:10.1144/GSL.SP.1999.154.01.02.

Sedlock, R.L., 1988, Tectonic setting of blueschist and island-arc terranes of west-central Baja California, Mexico: Geology, v. 16, p. 623, doi:10.1130/0091-7613(1988)016%3C0623:TSOBAI%3E2.3.CO;2.

Shervais, J.W., Choi, S.H., Sharp, W.D., Ross, J., Zoglman-Schuman, M., and Mukasa, S.B., 2011, Serpentinite matrix mélange: Implications of mixed provenance for mélange formation, *in* Mélanges: Processes of Formation and Societal Significance, Geological Society of America, doi:10.1130/2011.2480(01).

Shervais, J.W., Kimbrough, D.L., Renne, P., Hanan, B.B., Murchey, B., Snow, C.A., Zoglman Schuman, M.M., and Beaman, J., 2004, Multi-Stage Origin of the Coast Range Ophiolite, California: Implications for the Life Cycle of Supra-Subduction Zone Ophiolites: International Geology Review, v. 46, p. 289–315, doi:10.2747/0020-6814.46.4.289.

Shervais, J.W., Murchey, B.L., Kimbrough, D.L., Renne, P.R., and Hanan, B., 2005, Radioisotopic and biostratigraphic age relations in the Coast Range Ophiolite, northern California: Implications for the tectonic evolution of the Western Cordillera: Geological Society of America Bulletin, v. 117, p. 633, doi:10.1130/B25443.1.

Smye, A.J., Marsh, J.H., Vermeesch, P., Garber, J.M., and Stockli, D.F., 2018, Applications and limitations of U-Pb thermochronology to middle and lower crustal thermal histories: Chemical Geology, v. 494, p. 1–18, doi:10.1016/j.chemgeo.2018.07.003.

Spear, F.S., Thomas, J.B., and Hallett, B.W., 2014, Overstepping the garnet isograd: a comparison of QuiG barometry and thermodynamic modeling: Contributions to Mineralogy and Petrology, v. 168, p. 1059, doi:10.1007/s00410-014-1059-6.

Spear, F.S., Wolfe, O.M., Thomas, J.B., Hubbard, J.E., Castro, A.E., and Cheney, J.T., 2024, P–T Evolution of the Cyclades Blueschist Unit: Constraints on the Evolution of a Nascent Subduction System From Zr In Rutile (ZiR) and Quartz In Garnet (QuiG) Thermobarometry: Geochemistry, Geophysics, Geosystems, v. 25, p. e2023GC011121, doi:10.1029/2023GC011121.

Stacey, J.S., and Kramers, J.D. APPROXIMATION OF TERRESTRIAL LEAD ISOTOPE EVOLUTION BY A TWO-STAGE MODEL:

Stearns, M.A., Hacker, B.R., Ratschbacher, L., Rutte, D., and Kylander-Clark, A.R.C., 2015, Titanite petrochronology of the Pamir gneiss domes: Implications for middle to deep crust exhumation and titanite closure to Pb and Zr diffusion: TITANITE RECORD FROM THE PAMIR MID CRUST: Tectonics, v. 34, p. 784–802, doi:10.1002/2014TC003774.

Tuttle, L., and Henry, D.J., 2023, Metamorphic *P – T* paths of Archean granulite facies metasedimentary lithologies from the eastern Beartooth Mountains of the northern Wyoming Province, Montana, USA: constraints from quartz-in-garnet (QuiG) Raman elastic barometry, geothermobarometry, and thermodynamic modeling: European Journal of Mineralogy, v. 35, p. 499–522, doi:10.5194/ejm-35-499-2023.

Van Keken, P.E., Wada, I., Abers, G.A., Hacker, B.R., and Wang, K., 2018, Mafic High Pressure Rocks Are Preferentially Exhumed From Warm Subduction Settings: Geochemistry, Geophysics, Geosystems, v. 19, p. 2934–2961, doi:10.1029/2018GC007624.

Viete, D.R., Hacker, B.R., Allen, M.B., Seward, G.G.E., Tobin, M.J., Kelley, C.S., Cinque, G., and Duckworth, A.R., 2018, Metamorphic records of multiple seismic cycles during subduction: Science Advances, v. 4, p. eaaq0234, doi:10.1126/sciadv.aaq0234.

Vry, J.K., and Baker, J.A., 2006, LA-MC-ICPMS Pb–Pb dating of rutile from slowly cooled granulites: Confirmation of the high closure temperature for Pb diffusion in rutile: Geochimica et Cosmochimica Acta, v. 70, p. 1807–1820, doi:10.1016/j.gca.2005.12.006.

Wakabayashi, J., 2015, Anatomy of a subduction complex: architecture of the Franciscan Complex, California, at multiple length and time scales: International Geology Review, v. 57, p. 669–746, doi:10.1080/00206814.2014.998728.

Wakabayashi, J., and Dumitru, T.A., 2007, ^{40}Ar/^{39}Ar Ages from Coherent, High-Pressure Metamorphic Rocks of the Franciscan Complex, California: Revisiting the Timing of Metamorphism of the World's Type Subduction Complex: International Geology Review, v. 49, p. 873–906, doi:10.2747/0020-6814.49.10.873.

Wark, D.A., and Watson, E.B., 2006, TitaniQ: a titanium-in-quartz geothermometer: Contributions to Mineralogy and Petrology, v. 152, p. 743–754, doi:10.1007/s00410-006-0132-1.

Watson, E.B., Wark, D.A., and Thomas, J.B., 2006, Crystallization thermometers for zircon and rutile: Contributions to Mineralogy and Petrology, v. 151, p. 413–433, doi:10.1007/s00410-006-0068-5.

Wolfe, O.M., Spear, F.S., Thomas, J.B., Hasegawa, E.M., Libby, G.T., and Cheney, J.T., 2023, Pressure–temperature evolution of the basement and cover sequences on Ios, Greece: Evidence for subduction of the Hercynian basement: Journal of Metamorphic Geology, v. 41, p. 1119–1141, doi:10.1111/jmg.12738.

Zack, T., Moraes, R., and Kronz, A., 2004, Temperature dependence of Zr in rutile: empirical calibration of a rutile thermometer: Contributions to Mineralogy and Petrology, v. 148, p. 471–488, doi:10.1007/s00410-004-0617-8.